

The Photometric and Spectral Evolution of the 2008 Luminous Optical Transient in NGC 300¹

Roberta M. Humphreys², Howard E. Bond³, Alceste Z. Bonanos⁵, Kris Davidson², L. A. G. Berto Monard⁶, José L. Prieto^{7,9}, and Frederick M. Walter⁸

ABSTRACT

The 2008 optical transient in NGC 300 is one of a growing class of intermediate-luminosity transients that brighten several orders of magnitude from a previously optically obscured state. The origin of their eruptions is not understood. Our multi-wavelength photometry and spectroscopy from maximum light to more than a year later provide a record of its post-eruption behavior. We describe its changing spectral-energy distribution, the evolution of its absorption- and emission line-spectrum, the development of a bipolar outflow, and the rapid transition from a dense wind to an optically thin ionized wind. In addition to strong, narrow hydrogen lines, the F-type absorption-line spectrum of the transient is characterized by strong Ca II and [Ca II] emission. The very broad wings of the Ca II triplet and the asymmetric [Ca II] emission lines are due to strong

¹Based in part on observations with the NASA/ESA *Hubble Space Telescope* obtained at the Space Telescope Science Institute, and from the data archive at STScI, which is operated by the Association of Universities for Research in Astronomy, Inc., under NASA contract NAS5-26555; in part on archival data obtained with the *Spitzer Space Telescope*, which is operated by the Jet Propulsion Laboratory, California Institute of Technology, under a contract with NASA; in part on observations obtained with the 6.5-m Magellan Clay Telescope located at Las Campanas Observatory, Chile; in part on observations obtained with the SMARTS Consortium 1.3- and 1.5-m telescopes located at Cerro Tololo Interamerican Observatory, Chile, and in part on observations with VLT/UT1/ISAAC under ESO DDT proposal: 283.D-5019.

²Minnesota Institute for Astrophysics, 116 Church St SE, University of Minnesota, Minneapolis, MN 55455; roberta@umn.edu, kd@astro.umn.edu

³Space Telescope Science Institute, 3700 San Martin Drive, Baltimore, MD 21218; bond@stsci.edu

⁵Institute of Astronomy and Astrophysics, National Observatory of Athens, Athens GR-15236 Greece

⁶Klein Karoo Observatory (formerly Bronberg), PO Box 281, Calitzdorp 6660, Western Cape, South Africa

⁷Carnegie Observatories, 813 Santa Barbara St., Pasadena, CA 91101

⁸Department of Physics & Astronomy, Stony Brook University, Stony Brook, NY 11794-3800

⁹Hubble, Carnegie-Princeton Fellow

Thomson scattering in the expanding ejecta. Post-maximum, the hydrogen and Ca II lines developed double-peaked emission profiles that we attribute to a bipolar outflow. Between approximately 60 and 100 days after maximum, the F-type absorption spectrum, formed in its dense wind, weakened and the wind became transparent to ionizing radiation. We discuss the probable evolutionary state of the transient and similar objects such as SN 2008S, and conclude that they were most likely post-red supergiants or post-AGB stars on a blue loop to warmer temperatures when the eruption occurred. These objects are not LBVs.

Subject headings: stars: variables: other — galaxies: individual (NGC 300) — galaxies: stellar content — stars: individual (NGC 300 OT2008-1) — stars: winds, outflows — supernovae: general

1. Introduction: The Intermediate-Luminosity Transients

The numerous surveys for supernovae and transient variables have identified several non-terminal eruptive objects with maximum luminosities between novae and supernovae. Some have received a supernova designation (SN) and consequently have been called “supernova impostors” (Van Dyk et al. 2000). Many of these objects appear to be the “giant eruption” of a massive hot star perhaps similar to η Car (Humphreys & Davidson 1994, Humphreys et al. 1999). A few, like the 2008 optical transient in NGC 300 (Bond et al. 2009; Berger et al. 2009), discussed here, are apparently the unexplained outburst or eruption of a dust enshrouded progenitor of intermediate luminosity and mass, $\sim 10 - 17M_{\odot}$ (Bond et al. 2009; Gogarten et al. 2009). Prieto et al. (2009) have reported the presence of broad emission features in the mid-infrared spectrum of the transient similar to features seen in carbon-rich proto-planetary nebulae supporting their suggestion that the progenitor is actually a somewhat lower mass post-AGB star.

Related objects include SN 2008S (Prieto et al. 2008; Smith et al. 2009; Thompson et al. 2009) in NGC 6946, SN 2010da (Monard 2010; Khan et al. 2010a; Chornock & Berger 2010; Bond 2010) also in NGC 300, SN 2010dn in NGC 3184 (Smith et al. 2011), and the so-called “luminous red novae” PTF 10fqz (Kasliwal et al. 2011) in M99 and PTF 10acbp in UGC 11973 (Kasliwal et al. 2010). The red transient in M85 (Rau et al. 2007; Kulkarni et al. 2007) and the M31 red variable, M31 RV (see Bond & Siegel 2006; Bond 2011; and references therein), may have been similar outbursts, although they occurred in older stellar populations and presumably from lower-mass stars. The recently announced PSN J17592296+0617267 in NGC 6509 (Kelly et al. 2011) appears to be very similar to SN 2008S and the 2008 NGC 300 transient. These transients thus occur in intermediate-type and cool evolved stars

and possibly over a relatively wide mass range.

Given the very small sample, it is unclear if the causes of their instabilities and eruptions are physically related. A second group of transients may be more closely related to binary-star interactions. For example, the well-studied, peculiar eruptive star, V838 Monocerotis, famous for its spectacular light echo (Bond et al. 2003), was very different from a SN impostor or LBV-type eruption. Although V838 Mon later became enshrouded in dust, its light curve was also not like the other transients. The cause of its eruption is not known, but because of its unique properties, it has been speculated that it may have been the result of a stellar merger (Tylenda & Soker 2006). Two other Galactic examples are the nova-like V4332 Sgr (Martini et al. 1999) and V1309 Sco (Mason et al. 2010), which were both relatively red and cool during their outbursts.

Even though these intermediate-luminosity transients are rare, with the occurrence of a second, similar object in NGC 300 (SN 2010da) and the recent discovery that the outburst of V1309 Sco was caused by the merger of a contact binary (Tylenda et al. 2011), there is increased interest in these objects, the origins of their outbursts, and the nature of the progenitors. Bond (2011) has suggested calling all of these objects “intermediate luminosity red transients” (ILRTs) to distinguish them from true novae and LBVs.

This paper presents a detailed photometric and spectroscopic investigation of the 2008 NGC 300 optical transient (OT), “NGC 300 OT2008-1”. Hereafter in this paper we refer to it simply as “the OT” or “the transient”. In an earlier *Letter* (Bond et al. 2009), we presented a brief overview of its light curve and spectral characteristics. Berger et al. (2009) also published a discussion of their post-maximum spectral series in which they proposed a complex model for the its circumstellar ejecta and eruption. To provide more information on its post-eruption behavior, we describe here its spectral energy distribution, dust formation, and the evolution of the optically thick wind and outflow from maximum to late times. Our multi-wavelength observations and the light curve are presented in the next section. The color-magnitude diagram and stellar-population characteristics in the OT’s immediate environment are described in §3. Its changing spectral energy distribution and dust formation, the energetics of the eruption, and the luminosity and mass of the progenitor are discussed in §4. In §5 and 6 we describe the behavior of the emission and absorption lines as the eruption declined, the development of the bipolar outflow, and the transition to an optically thin wind. In the final section we discuss some possible explanations for the outburst and comment on the transient’s evolutionary state.

2. Multi-wavelength Observations and Data Reduction

Our observations include ground-based CCD imaging and photometry, near-infrared photometry, low- to moderate-resolution optical and near-infrared spectroscopy, *Hubble Space Telescope* (*HST*) imaging, and *Spitzer* mid-infrared photometry (Prieto 2008). We conducted a program of photometric monitoring of the transient from 2008 May 15 until 2009 June 22, and spectroscopy from 2008 May 15 to 2009 January 16 with the 1.3- and 1.5-m telescopes at Cerro Tololo Interamerican Observatory (CTIO), operated by the SMARTS consortium¹. These spectra were supplemented by echellette spectra from the Magellan telescope and near-infrared spectra from the VLT.

2.1. Optical and Near-Infrared Imaging and Photometry

The outburst was discovered by Monard (2008) at broad-band magnitude 14.3, using his 0.3-m telescope equipped with a CCD camera, on a frame obtained on 2008 May 14 (UT). An earlier frame, taken on 2008 April 24, and examined after discovery of the eruption, showed the transient at ~ 16.3 mag. It was fainter than 18 mag on 2008 February 8, and on all previous monitoring observations obtained by Monard.

Our program of systematic photometric monitoring began on 2008 May 15. These data were obtained by Chilean service observers with the 1.3-m SMARTS telescope at CTIO with the ANDICAM optical/near-IR direct camera (DePoy et al. 2003), which simultaneously obtains optical frames with a CCD detector and near-IR frames with an IR detector. We used the *BVRI* filters of the Johnson-Kron-Cousins system in the optical, and standard *JHK* filters for the near-IR.

The *BVRI* frames were processed through the SMARTS reduction pipeline at Yale University, which performs bias subtraction and flat-fielding. We then used standard aperture-photometry routines in IRAF² to determine magnitudes differentially with respect to a nearby comparison star. The comparison star is located at J2000 coordinates (USNO-NOMAD catalog) RA = 00:54:39.545, Dec = $-37:37:14.79$. The magnitudes of the comparison star were calibrated on seven photometric nights by reference to standard stars published

¹SMARTS is the Small and Medium Aperture Research Telescope System; see <http://www.astro.yale.edu/smarts/>

²IRAF is written and supported by the IRAF programming group at the National Optical Astronomy Observatories (NOAO) in Tucson, Arizona. NOAO is operated by the Association of Universities for Research in Astronomy (AURA), Inc. under cooperative agreement with the National Science Foundation

by Landolt (1992), and are $V = 16.07$, $B - V = 0.75$, $V - R = 0.42$, and $V - I = 0.82$ with errors of ± 0.02 – 0.03 mag. The JHK magnitudes are also differential with respect to the same comparison star, calibrated using its 2MASS photometry. The J2000 position of the OT, based on astrometry of ANDICAM frames calibrated against the USNO-NOMAD catalog, is RA = 00:54:34.51, Dec = $-37:38:31.4$, with errors in each coordinate of $\pm 0''.2$.

The journal of observations and the multi-wavelength photometry is in Table A1 in the Appendix in the electronic edition. Figure 1 shows the $BVRIJHK$ light curve. The rise to maximum was poorly covered, but it was much more rapid than the subsequent slower decline. The brightest V magnitude we measured was 14.69, on the first night of SMARTS observations (2008 May 15), corresponding to an absolute visual magnitude $M_{V,0} = -12.2$ to -13.1 for the adopted distance (see §3) and reddening in the range $E(B - V) = 0.1$ to 0.4 (see §4). Following maximum light, the transient declined smoothly in brightness at all wavelengths, but with a noticeable change in slope in 2008 September. The R magnitudes did not fade as rapidly as in the other bandpasses, due to strong $H\alpha$ emission.

In Figure 2 we plot the changes in the color indices $B - V$ and $V - K$ with time. The $V - K$ color became steadily redder as the transient evolved, but with a change to a shallower slope in 2008 September due to the change in slope of the V magnitude. $B - V$ also became redder (but note the expanded scale for this color in Fig. 2) until 2008 August, but then trended back toward bluer colors. These changes in color are discussed further in §4.

2.2. Spectroscopy

We regularly obtained low- and moderate-resolution spectra of the transient throughout its outburst from 2008 May 15 to 2009 January 16, using the long-slit Ritchey-Chretien (RC) spectrograph on the SMARTS 1.5-m. We used a $1''.5$ slit and a variety of gratings, yielding spectral resolutions from 3.1 to 17.2 Å, and covering the spectral range 3150 to 9350 Å (see Table 1). Each observation consisted of three integrations, which were median filtered to remove cosmic rays and then summed. Each set of images was wavelength calibrated with a Ne-Ar or Th-Ar arc lamp. The images were bias-subtracted, trimmed, and flattened using dome flats obtained each night. The spectra were extracted by fitting a Gaussian in the spatial dimension at each column in the CCD. The net counts at each pixel are the integrated counts in the Gaussian, less the interpolated background fit on either side of the spectrum. The spectrophotometric standard, Feige 110, was observed each night to convert the counts to flux. Due to seeing-related slit losses and possible transparency changes during the night we do not obtain absolute fluxes, but rather merely recover the shape of the continuum. We correct to true fluxes by scaling them to match the observed

BVRI magnitudes, interpolating as necessary. The observation dates and grating used are summarized in Table A2 in the Appendix in the electronic edition.

We also obtained moderate-resolution spectra with the Magellan 6.5-m telescope and MagE echellette spectrograph (Marshall et al. 2008) on 2008 July 6, August 30, and September 1. These spectra cover the wavelength region from 3100 Å to 1 μm. The integration times were 2 × 800 s on July 6 and 900 s each on August 30 and September 1. The 0′.7 slit yielded a resolving power $R \simeq 6000$, corresponding to a resolution of 1.5 Å at the Ca II triplet and 1.1 Å at Hα. The MagE spectra were reduced, extracted and wavelength calibrated with an IDL pipeline written by G. Becker (version 1.01), which implements optimal extraction techniques (e.g., Kelson 2003). A fourth MagE spectrum was obtained on 2009 June 5, more than a year after the eruption. With a combined 3000 s integration, there is no continuum and the only emission lines detected are Hα and the Ca II triplet.

We also obtained Director’s Discretionary Time at the European Southern Observatory for near-infrared spectroscopy with the Infrared Spectrometer and Array Camera (ISAAC) on the VLT/UT3 telescope on 2009 July 19–23, more than a year after maximum. These low-resolution spectra were observed at central wavelengths 1.65 μm, 2.2 μm, and 3.55 μm, and a medium-resolution spectrum was obtained at 2.2 μm. Due the faintness of the object (see Table A1), the spectra have low S/N. Brγ and Paα are present in emission.

3. The Stellar Environment

As we described in Bond et al. (2009), the *HST* archive contains two sets of deep frames made before the outburst that fortuitously cover the OT site, obtained with the Wide Field Channel (WFC) of the Advanced Camera for Surveys (ACS) and the F435W, F475W, F555W, F606W, and F814W filters. These observations were made on 2002 December 25 (GO-9492, PI: F. Bresolin) and on 2006 November 8–10 (GO-10915, PI: J. Dalcanton). The frames were obtained in three different pointings in a spiral arm of NCG 300 lying to the northwest of the nucleus. Field 5 in Bresolin et al. (2005) includes the site of the transient, one of the Dalcanton frames largely overlaps it, and a second one is adjacent to it on the SE side, as shown in Gogarten et al. (2010, their Fig. 1). We also obtained two observations during the outburst in our *HST* Director’s Discretionary (DD) program GO-11553 (PI: H. Bond). The DD observations were made on 2008 June 9 and September 1, using the Wide Field Planetary Camera 2 (WFPC2) with F450W and F814W filters. We used these data to locate the OT site precisely in the pre-eruption frames and search for a progenitor object. Remarkably, no progenitor star was detected in any of the ACS frames, to a magnitude limit of 28.5 in the F606W image.

These deep pre-outburst frames can be used to study the surrounding stellar population, and thus make inferences about the possible nature of the progenitor star. We made brief comments about the stellar environment in Bond et al. (2009), including the fact that there are several blue main-sequence stars within $2''.5$ (23 pc) of the OT site with initial masses as high as $\sim 14 M_{\odot}$. An extensive study of the stellar populations and star-formation history around the OT was made by Gogarten et al. (2009), based on their independent analysis of the same *HST* material. Due to the presence of stars in the immediate vicinity of the OT with ages of only ~ 8 – 13 Myr, they concluded that the progenitor was likely to have had an initial mass in the approximate range 12 – $17 M_{\odot}$.

Our independent photometric analysis of the archival *HST*/ACS material was done using techniques described in detail by Anderson et al. (2008). Because our findings largely verify those reported by Gogarten et al. (2009), we give only a brief summary here. We prepared stacked images by combining all of the available ACS frames. The combined images cover slightly more than the equivalent of two ACS/WFC fields, each of which is $202'' \times 202''$ or about 1.8×1.8 kpc at the distance of NGC 300. We then carried out stellar photometry on these combined images, calibrated on the Vega-mag system, as described by Bedin et al. (2005), and adopting the ACS/WFC encircled-energy function and photometric zero-points given by Sirianni et al. (2005).

Figure 3 shows the resulting color-magnitude diagrams (CMDs) for all stars detected in the stacked ACS frames (the black points in the diagrams). The left-hand frame shows I vs. $V - I$ (m_{F814W} vs. $m_{F606W} - m_{F814W}$), and the right-hand frame shows I vs. $B - I$ (m_{F814W} vs. $m_{F475W} - m_{F814W}$). The CMDs reveal a combination of a young population (the nearly vertical plumes of blue main-sequence stars, blue loop stars, and red supergiants), an intermediate-age population (the AGB stars lying above the red-giant tip), and an underlying older population of numerous red giants.

The tip of the red-giant branch (TRGB) is well-defined in Figure 3, and allows us to determine the distance to NGC 300 using this well-known method (e.g., Madore & Freedman 1995). We first transformed our data onto the Johnson-Kron-Cousins VI system, using relations given by Sirianni et al. (2005), and then determined the luminosity function (LF) of the RGB stars. We then applied a Sobel filter to the LF, using techniques described by Sakai, Madore, & Freedman (1996), to determine the I magnitude of the TRGB. We find $I_{\text{TRGB}} = 22.60 \pm 0.10$, with the quoted error being the HWHM of the Sobel peak. Adopting $E(B - V) = 0.037$ from Gogarten et al. (2009) and $A_I = 2.0E(B - V)$, we obtain $I_{0,\text{TRGB}} = 22.53 \pm 0.10$, including a ± 0.02 mag uncertainty associated with the reddening estimate. Adopting an absolute magnitude $M_{I,\text{TRGB}} = -4.04 \pm 0.12$ (e.g., Rizzi et al. 2006), we derive a distance modulus of $(m - M)_0 = 26.57 \pm 0.14$, corresponding to 2.03 ± 0.13 Mpc.

Our result is in good (1σ) agreement with the distance modulus adopted in an extensive discussion of the NGC 300 literature by Gogarten et al. (2010), $(m - M)_0 = 26.43 \pm 0.09$ (1.93 Mpc).

To better characterize the stellar population in the vicinity of the OT, we consider only the stars located within a 500×500 pc square centered on its position. The CMD for these stars is shown in Figure 4 (left panel), with stars lying in different evolutionary states indicated by the color-coding, as described in the caption. In the right panel, we show the spatial distribution of the various types of stars by zooming in on a 200×200 pc square with the same color-coding.

This diagram reveals several features. First, the entire field is underlain by a substrate of old red giants (dark-red points). There is also a fairly uniform scattering of blue main-sequence and blue-loop stars (slate-blue and bright-blue points) across the field, but with a slight gradient toward higher stellar densities to the west (right-hand) side of the field. There is little evidence among these blue stars for clustering or young associations, although there *are* several obvious clusters and associations not far outside the field in the west and southwest direction. Several of the young main-sequence stars lie within $\sim 2''$ – $3''$ (~ 18 – 27 pc) of the transient’s site, as already noted by Bond et al. (2009) and Gogarten et al. (2009). The rarer red supergiants (orange points) and AGB stars (bright-red points) are distributed approximately uniformly across the field. This figure thus reveals a mixed stellar population in the transient’s immediate vicinity.

4. The Spectral Energy Distribution, Energetics of the Eruption, and Luminosity and Mass of the Progenitor

Figures 5 and 6 show the transient’s spectral energy distribution (SED) at maximum light and its subsequent evolution from maximum to 2009 June 22, more than a year later.

The observed $BVRI$ and JHK magnitudes from day 2 in the eruption are shown in Figure 5. The same magnitudes are plotted corrected for the mean interstellar extinction, $A_V \approx 0.3$ mag, for NGC 300 (Gieren et al. 2005) and from the field stars near the transient (Gogarten et al. 2009). We also show the photometry corrected for $A_V = 1.2$ mag assuming an intrinsic color ($B - V_0 \simeq 0.3$ to 0.5 mag) appropriate to its F-type absorption spectrum at maximum (Bond et al. 2009). $E(B - V)$ is then ~ 0.4 mag from its observed $B - V = 0.8$ at maximum. The 7500 K blackbody, fit through the latter points, is consistent with the F-type absorption spectrum observed at maximum and for several months afterwards. The absorption spectrum, discussed in §5 and 6, very likely originates in a dense wind, but could

also correspond to the progenitor’s actual photosphere. In either case, 7500 K is the apparent temperature of the region from which the visual light is escaping. An energy distribution of comparable temperature cannot be fit to the photometry corrected for the lower extinction value. A much lower temperature of 4000–4500 K, inconsistent with the spectrum, would be necessary to fit the $B - V$ color corrected for the lower extinction, but even then it is not a good fit to B and does not match the R and I magnitudes. We therefore adopt $A_V = 1.2$ mag for this discussion. This higher A_V may simply be due to higher interstellar reddening for the OT than for the surrounding field stars, but as we show here, it is more likely due to circumstellar extinction from dust.

In Figure 5, a 7500 K blackbody fit to the B , V , and R magnitudes leaves a small excess at I and J above the blackbody which, at these wavelengths, is due to free-free emission in the star’s wind. The contribution from a 7500 K free-free curve is also shown. The adopted temperature for the free-free emission is somewhat arbitrary, but it does not make much difference; a T_{ff} in the 5000–10000 K range would look very similar. The combined blackbody plus free-free fit leaves a small excess at H and a large excess at K , presumably due to dust. If we assume that the correction due to interstellar extinction is 0.3 mag and the 0.9 mag difference is circumstellar, then about half of the total flux is absorbed by dust. We can therefore model the dust contribution assuming that the integrated flux from dust is 50% of the blackbody plus free-free flux, and the combined flux plus dust must match the K -band magnitude. These conditions are fulfilled by the 715 K dust contribution shown in Figure 5. The resulting SED matches the $BVRI$ and JK fluxes very well. The H -band magnitude was not used in this fit, but is also matched quite well. This result suggests that some dust either survived the eruption, or was formed during the outburst.

With an A_V of 1.2 mag, the luminosity of the OT at maximum was $1.5 \times 10^7 L_{\odot}$ with a photospheric radius of ~ 11 AU for an apparent temperature of 7500 K. The 715 K dust is at about 1500 AU (9 light days) from the star. The K -band photometry shows considerable variability between day 2 and day 33 (Figure 2), as much as 0.2 to 0.3 mag in one day (see Table A1). Although it is tempting to attribute this to variable dust formation immediately after the eruption, variations of this size in less than a week would be hard to explain. Furthermore, with expansion velocities of 500–600 km s $^{-1}$ at maximum (Berger et al. 2009), the ejecta from the eruption would require more than a year to reach this distance. *Therefore, the dust must be a remnant from the star’s previously obscured state.* In their discussion of the carbon-rich mid-IR emission feature and the SED at day 93 (see below), Prieto et al. (2009) also concluded that the corresponding dust survived the eruption.

Figure 6 shows the observed SED at several different times after maximum, along with the pre-outburst infrared SED (Prieto 2008) and the mid-IR emission feature observed on

2008 August 14 (Prieto et al. 2009). As the OT faded, it also became redder, but its characteristic F-type absorption-line spectrum was still weakly present in mid-August 2008 (day 90); see §5 and §6. We therefore attribute the redder color to increased dust formation and circumstellar reddening. Following the discussion above, we estimate the combined interstellar and circumstellar extinction from the observed $B - V$ color and F-type spectrum to determine the extinction-corrected SEDs also shown in Figure 6. The adopted values of A_V are included in the figure caption. By 2008 September (day 117) the absorption spectrum was clearly gone and the $B - V$ color was bluer, although $V - K$ was redder. We adopted the last value of A_V for the later dates. After that, the SED rapidly becomes much steeper in the visual. The change in the shape of the SED, the disappearance of the absorption spectrum, and the bluer $B - V$ correspond to the change in the slope of the visual light curve in Figure 1 beginning in 2008 September. These changes are very likely due to the transition in the dominant radiation field described in §5 and §6. By the time of our last visual measurement, day 405, the transient was still more luminous than the pre-outburst *Spitzer* data (Prieto 2008) shown in Figure 6.

Its pre-eruption infrared SED indicates that the optically obscured progenitor had an intrinsic luminosity of $6.3 \times 10^4 L_\odot$, at our adopted distance (2.02 Mpc) for NGC 300, corresponding to $M_{\text{bol}} \simeq -7.3$, placing it just above the AGB limit at $M_{\text{bol}} \simeq -7.0$. At maximum light, with its F-type absorption spectrum probably due to the formation of an optically thick wind or envelope, its bolometric correction will be near zero, so that $M_V \simeq M_{\text{bol}}$ at maximum. With an M_V of -13.1 ($A_V \approx 1.2$) at maximum³, the OT thus increased its total luminosity by about 6 mag or a factor of 250, during its eruption.

The energy released in the eruption, however, was relatively modest compared to other non-terminal eruptions. Integrating over the visual light curve, corrected for extinction ($A_V \simeq 0.3$ to 1.2 mag), beginning with the initial detection on 2008 Apr 24, and assuming that the bolometric correction is zero, we find that the total emitted energy was $1\text{--}2 \times 10^{47}$ ergs. Almost all of this energy was released in the first two months. This is considerably less than the luminous energy, $\sim 10^{50}$ ergs, emitted in η Car’s famous great eruption, but it may be comparable to its second, lesser eruption in the 1890’s, which released 6×10^{47} ergs during its 7-year outburst. If the ratio of luminous to kinetic energy is near unity, as in η Car, then with a wind speed of $\sim 75\text{--}100$ km s⁻¹ (see §6), the total mass lost by NGC 300 OT2008-1 was $1\text{--}2 M_\odot$. However, this is very likely an upper limit. For example, in the classical LBV “eruptions” the luminous energy is 10–100 times greater than the kinetic energy. A realistic estimate of the mass shed in the eruption is therefore somewhere between ~ 0.1 and $1 M_\odot$.

³With $A_V = 0.3$, M_V at maximum was -12.2 .

Comparison with evolutionary tracks for solar metallicity, with and without rotation (Maeder & Meynet 2000), suggests an initial mass of 10–15 M_{\odot} for the progenitor star based on its pre-outburst luminosity, assuming that it is an evolved red supergiant (RSG) or post-RSG star (Bond et al. 2009). Note that the progenitor is just above the AGB limit. Using color-magnitude diagrams to age-date the surrounding population, Gogarten et al. (2009) concluded that the progenitor’s initial mass was between 12 and 17 M_{\odot} . Our inspection of the spatial distribution of the different stellar populations in the immediate neighborhood of the progenitor in §3 is inconclusive. It could have originated from a fairly massive star or from an intermediate-mass star of $\sim 5\text{--}9 M_{\odot}$ on the AGB. The detection of mid-IR emission features attributed to hydrocarbons (Prieto et al. 2009) may suggest that the progenitor was a post-AGB star, similar to proto-planetary, and may have evolved from lower masses.

5. Evolution of the Spectrum

The distinguishing characteristics of the transient’s optical spectrum are its strong, narrow H α emission line, strong Ca II triplet emission, and the rare [Ca II] emission lines near $\lambda 7300 \text{ \AA}$. Our first spectrum, obtained at maximum light, is shown in Figure 2 in our earlier *Letter* (Bond et al. 2009). Although the resolution of this first spectrum is relatively low (17 \AA), it also shows several absorption lines that resemble the spectrum of a luminous F-type supergiant with strong H and K lines, a weak G-band, Na I D line blend, and absorption lines, especially around 4175 \AA and 4144 \AA that are blends of lines that are strong in F-type supergiants. The O I blend at 7774 \AA , a strong luminosity indicator for A- and F-type supergiants (Osmer 1972), is also present in absorption.

An apparent F-type supergiant spectrum is expected in an eruption that produces an optically thick wind or envelope. Suppose that the star’s basic radius, in the absence of a wind, corresponds to an effective temperature above $\sim 8000 \text{ K}$, with a fixed luminosity. If a sufficiently dense outflow arises, the wind becomes opaque, so that the effective photosphere is then located well outside the star. Under these conditions, of course an increase in the wind density tends to enlarge the photospheric radius, thereby reducing the apparent temperature. However, the relevant opacity declines precipitously below 7500 K; therefore a photospheric temperature below 7000 K requires a very high wind density. This behavior was described by Davidson (1987), who emphasized that a broad range of mass-loss rates (even in the logarithmic sense) all give apparent temperatures between 6500 and 7500 K. Since the effective gravity is near zero, the resulting spectrum resembles an intermediate-temperature supergiant. This is why LBVs/S Doradus variables at maximum have apparent A- to F-type supergiant absorption spectra and energy distributions (Humphreys & Davidson 1994).

Thus, the F-type absorption spectrum is most likely produced in the transient’s dense wind or it could represent the progenitor’s photosphere. The absorption lines do weaken with time and are eventually gone by later times. These apparent changes in what may be a cool dense wind are discussed later.

5.1. The Hydrogen and Ca II Emission-line Spectrum

The spectrum is dominated by a very strong $H\alpha$ emission line. Its equivalent width increased by more than a factor of 20 from maximum light through 2008 December, due primarily to the decreasing level of the continuum as the object faded. The integrated line flux, however, shows that the strength of $H\alpha$ did indeed increase, reaching a maximum 50–60 days after maximum light (2008 July), and declined thereafter. At maximum light, 2008 May 15, the $H\alpha$ profile had a FWHM of 1050 km s^{-1} , but became narrower with time, and a year later, in 2009 June, the FWHM was only 300 km s^{-1} . The later $H\alpha$ profiles observed with our highest-resolution RC grating and the echellette spectra also show relatively symmetric, prominent Thomson-scattering wings. These are produced in the wind, with wavelengths corresponding to velocity shifts of the order of $\pm 900\text{--}1000 \text{ km s}^{-1}$ (Figure 7), due to scattering off the electrons, not to bulk Doppler motions. The scattering wings may always have been present in the early spectra, but only became apparent as the continuum level decreased.

The Ca II triplet and the unusual [Ca II] emission lines are present in all of our spectra. These lines are indicative of an extensive circumstellar medium and provide information on conditions in the ejecta, which, as we describe here, changed with time as the eruption declined. The integrated fluxes for the triplet lines noticeably increase in strength, reaching a maximum in 2008 July, like $H\alpha$, while the integrated fluxes for the [Ca II] lines continuously decrease in strength from May to December. The Ca II triplet emission lines are formed in the star’s ejecta by radiative de-excitation from the strong Ca II H and K absorption upper levels, and are observed in the spectra of the winds or envelopes of the warm hypergiants, but are not commonly observed in the spectra of the dense winds of LBVs at maximum, their optically thick wind state. Ca II has a low ionization potential and is suppressed in the presence of UV radiation. The transition that produces the triplet emission leaves the ions in the upper level for the [Ca II] forbidden lines. These ions are normally collisionally de-excited back to the ground state that produces the H and K lines, unless the density is sufficiently low. For these reasons the [Ca II] emission lines are rarely seen in stellar spectra.

We can estimate the number of photons that are radiatively de-excited from the ratio of the combined equivalent widths (or fluxes) of the [Ca II] lines and the Ca II triplet, multiplied by the expected ratio of the corresponding continuum fluxes at 7300 \AA and 8600 \AA ,

respectively. For this calculation, we assumed a 7000 K blackbody. At maximum light in 2008 May, we find that about 1/4 of the photons produced the forbidden lines by radiative de-excitation to the ground state. This is similar to the results for the ejecta and winds of the much more luminous stars IRC +10420 (Jones et al. 1993; Humphreys et al. 2002) and Var A in M33 (Humphreys et al. 2006). The [Ca II] lines are thus produced in a region of much lower density than normally found in the atmospheres and winds of luminous supergiants, and therefore originate outside the dense wind that formed during the eruption. But that changed with time. In later spectra, the ratio declined to one-tenth in 2008 August through September and to approximately one-twentieth by 2008 November. This rapid decline in the photon ratio could be due to an increase in the density in the ejecta where the [Ca II] lines are formed, or to an increase in the ionizing flux, as discussed below and in §6.

Prieto et al. (2009) and Smith (2009) have suggested that the [Ca II] emission lines are instead due to dust destruction, which presumably populates the necessary upper levels. However, the spectrum of the transient has very strong Ca II H and K absorption lines which will populate the upper level, and so far, no one has done the necessary analysis to demonstrate that dust destruction will do likewise.

5.1.1. *The Double-Peaked Emission-Line Profiles*

In the post-maximum spectra both the Ca II triplet and H α show prominent double or split emission lines with asymmetric profiles (see Figures 7 and 8). Double-peaked emission is normally attributed to either a bipolar outflow or a rotating disk. In this case, with an ongoing eruption, they are most likely being formed in the wind or ejecta. A pre-existing disk would very likely have been disrupted during the eruption. An alternative model is self-absorption superposed on a broad emission line. It is easy to invoke self-absorption and it probably cannot be entirely ruled out in this case, but it is very dependent on the geometry. Furthermore, it is difficult for H α to be self-absorbed, and requires that the $n = 2$ level be populated in the intervening material. Given the similarities of the H α and Ca II triplet profiles, we would expect them to have the same origin. The unequal, asymmetric profiles which change with time, plus the evidence for blue and red-shifted multiple components discussed in §6, in our opinion, favor an outflow interpretation.

The double-peaked Ca II emission lines were first noticed in our spectrum of 2008 June 20, obtained with our lowest-resolution grating (Gr 13). All three lines were clearly double, with prominent blue and red components and an easily recognizable absorption minimum. The Ca II profiles in the echellette spectra from 2008 July 6 and August 30/September 1, shown in Figure 8, are resolved and reveal a complex and variable structure with evidence

for secondary emission components in addition to the prominent blue and red peaks. The triplet lines are also asymmetric to the red, similar to the [Ca II] lines; see §5.2. In our RC spectra the triplet lines all appear single after mid- August 2008.

The first evidence that the strong $H\alpha$ line was double, with a broadened top and two maxima of about equal strength, appears in our 2008 June 21 RC moderate-resolution spectrum. The $H\alpha$ emission line in the three echellette spectra from 2008 July/August shows two well-resolved components (see Figure 7), with evidence for secondary emission features similar to those observed in the Ca II triplet. The $H\alpha$ profile in the last echellette spectrum, a year later, from 2009 June 5 still shows a prominent double-peaked structure with evidence for multiple components. $H\beta$ in the echellette spectra from 2008 also shows similar double profiles. Although the other hydrogen lines may appear essentially single, inspection of their profiles shows evidence for broadening due to other emission components. $Br\gamma$ and $Pa\alpha$ in the low-resolution ISAAC 2 μm spectrum from 2009 July are in emission and $Br\gamma$ has a double-peaked profile.

The series of moderate-resolution RC spectra reveals some interesting short-term variability in the strength of the $H\alpha$ line and the double-peaked signature. For example, in Figure 9, the 2008 September 10 spectrum shows a well-developed double profile with two clearly separate components and an absorption minimum. In the spectrum from September 13, however, with the same grating, the separation in the $H\alpha$ profile was barely detectable as a broadening or small bump on the red side of the line. But then only three days later (September 16) the $H\alpha$ profile was clearly double again and the line was even stronger than on September 10. On September 27, the signature of the split profile was again weaker and the overall flux in the $H\alpha$ line much weaker. After that the hydrogen emission profiles were very consistent with little evidence for variability in the profile shape. $H\alpha$ continued to show evidence for the double-peaked profiles until our last observation with this grating in 2009 January. These short-term changes may be indicative of variations in the outflow. They also correspond to the change in the slope of the light curve and the SEDs, §4, and the transition to an optically thin state, §6.

The heliocentric Doppler velocities measured from the echellette spectra for the components of the double Ca II triplet and the $H\alpha$ line are given in Tables 2 and 3, respectively. The Ca II and $H\alpha$ profiles show considerable complexity, with evidence for additional emission components which appear as shoulders or secondary bumps on the primary blue and red peaks. Comments and notes about these features are included in the tables. Because of the complexity of many of these profiles, a program to automatically fit Gaussians to the profiles did not give satisfactory results. To measure the velocities of the two components, we therefore first measured the maximum or central wavelength of the stronger blue compo-

ment by bisecting the very top of the profile. We then fit a Gaussian to the blue component assuming a symmetric profile about the central wavelength. This was then subtracted from the line to estimate the central wavelength of any secondary features or shoulders. The same process was followed for the red component. We have also included the Doppler velocities for the H α blue and red peaks measured in the RC spectra. We followed a process similar to that described above to measure the velocities of the two primary components and adopted the intersection of the curves for the blue and red components for the absorption minimum. The secondary emission features are not as evident in these moderate-resolution spectra.

The mean velocities measured for the absorption minimum in the double-peaked Ca II and H α lines from the echellette spectra of $192 \pm 2 \text{ km s}^{-1}$ and $202 \pm 6 \text{ km s}^{-1}$, respectively, are consistent with each other and compatible with the OT's expected radial velocity of $\approx 190 \text{ km s}^{-1}$ from NGC 300's rotation curve at its location in the galaxy (Marcelin et al. 1985), and with the velocities of other emission lines in Table 4.

5.2. The [Ca II] Lines

The [Ca II] lines, formed in a very low-density region, do not show any evidence for double-peaked profiles, but the profiles of both lines are asymmetric to the red and have Thomson scattering wings extending from approximately ± 250 to $\pm 300 \text{ km s}^{-1}$; see Figure 10. Berger et al. (2009) attributed the asymmetric profiles to inflowing gas on the red side and absorption by intervening material on the blue side of the lines; however, self-absorption is highly unlikely, if not impossible, for a forbidden emission line. A physically more realistic explanation is the effect of electron scattering on the profiles, as first demonstrated by Auer & Van Blerkom (1972). They showed that radiation transfer through an expanding envelope will substantially alter the shape of the profiles. For a line formed by recombination, as in the case of the [Ca II] lines, the only source of opacity is the free electrons. With electron-scattering optical depths of ~ 1 , the profiles will be asymmetric with extensive wings to the red of the expected line center. See Hillier (1991) for examples of model profiles with the effects of electron scattering which closely resemble the [Ca II] lines in the transient. SN 2010dn shows similar asymmetric [Ca II] profiles (Smith et al. 2011).

After mid-June 2008 (Table 4), the [Ca II] Doppler velocities measured from the echellette spectra and the RC spectra with grating (#58) show little evidence for variability, and yield mean velocities of $207 \pm 2.6 \text{ km s}^{-1}$ and $226 \pm 7.7 \text{ km s}^{-1}$ for the $\lambda 7291 \text{ \AA}$ and $\lambda 7323 \text{ \AA}$ lines, respectively.

5.3. Other Emission Lines

Many weaker emission lines are present in these spectra. Several are visible in the RC spectra, but they are obviously much more numerous in the echellette spectra. These lines became relatively stronger at later times. They may have always been present but become more apparent as the continuum declined with time, although most were no longer detectable after early 2008 September. Most of these lines are identified with Fe II and [Fe II], formed in the star’s wind. Not surprisingly, emission lines from the Paschen series of hydrogen are present. The presence of He I, O I, [O I], and Na I D in emission is of more interest and is discussed here.

The O I blend at $\lambda 8446 \text{ \AA}$ is present in emission in the RC spectra beginning with those obtained in 2008 July, and in the echellette spectra, and is still present in the RC spectra from later times until 2008 December. In their higher-resolution echelle spectra, (Berger et al. 2009) find the O I $\lambda 8446$ line initially in absorption, which transitions to an emission line in 2008 July/August. This is similar to the behavior of the Na I D lines, described below. Although the $\lambda 8446$ line appeared to increase in strength with time in our spectra, the total flux in the line remained essentially constant. This emission line is observed in novae, nova-like objects, AGNs, and Seyfert galaxies, and given the lack of any other O I emission lines in the spectrum, its most likely origin is $\text{Ly}\beta$ pumping by fluorescence (Bowen 1947; Grandi 1980). Berger et al. (2009) also noted the connection with $\text{Ly}\beta$. This is the only emission line that shows a blueshift in its velocity with time (Table 4), which may be related to the fluorescence with $\text{Ly}\beta$. The [O I] lines at $\lambda 6300 \text{ \AA}$ and $\lambda 6363 \text{ \AA}$ are also identified in two echellette spectra, but are not seen in later spectra. Berger et al. also noted a one-time appearance in their echelle spectra from 2008 August 23.

Similarly, the He I emission line at $\lambda 5876 \text{ \AA}$ is observed in the RC spectra, beginning with those obtained in 2008 June. Additional, relatively weak, He I lines at $\lambda \lambda 7065, 6678, 3964$ (blended with Fe II) and $\lambda 3888$ (probably blended with H ζ) are also identified in the echellette spectra. These weaker He I lines are not apparent in the RC spectra. Both the O I $\lambda 8446$ emission line and the He I emission lines require UV photons for their excitation. But, unlike the O I line, the strong He I $\lambda 5876$ line slowly weakened with time and was no longer observed in spectra obtained after 2008 October 1.

The Na I D lines interestingly change from a strong absorption feature in the echellette spectrum from 2008 July 6 to emission in the August 30–September 1 spectra shown in Figure 11⁴. In the RC spectra, the Na I D lines are observed in absorption at maximum

⁴Berger et al. (2009) assumed the Na I D line absorption lines are interstellar in origin. However, strong

(2008 May 15) and in the spectra from June 20 and July 18. They are not apparent either in emission or absorption in a spectrum from August 23, but are in emission in the spectrum from September 8 obtained with the same grating. With low resolution it is uncertain if they are present in emission after that. Thus in about one month, ~ 100 days after maximum, the Na I D lines went from absorption to emission. The line profile from August 30–September 1 shows some weak absorption superposed on the emission (Figure 11). Measurement of the total flux in the absorption components show that they decreased by about a factor of two between July 6 and August 30. So, about half the flux previously in the absorption lines was now in emission. The O I $\lambda 8446$ line also transitioned from absorption to emission during the same time period (Berger et al. 2009). Since the other absorption lines were also weakening with time, we suggest that *the expanding envelope was becoming more transparent to the ionizing photons.*

The velocities measured from these different lines are summarized in Table 4. All velocities are heliocentric. The mean velocity of 40 emission lines in the 2008 August 30/September 1 echellette spectra is $+200 \pm 4.4 \text{ km s}^{-1}$.

5.4. The Absorption Spectrum

Several absorption lines typical of F-type supergiants and optically thick winds are present in the spectrum at maximum light, although they appear to weaken with time in the low-resolution RC spectra. These lines include several luminosity-sensitive features such as the O I triplet at $\lambda 7774 \text{ \AA}$, and the Fe II–Ti II blends at $\lambda 4172\text{--}4178 \text{ \AA}$, plus Ca II H and K, Ca I $\lambda 4226 \text{ \AA}$, the Na I D lines, and a weak G-band. These same lines, plus additional lines of Sr II, Ti II, Sc II, and Mn I, appear relatively strong in the echellette spectrum from 2008 July 6, but at significantly lower velocities (Table 4), and are no longer apparent in the August 30–September 1 spectra. Their mean radial velocity in the July 6 spectrum from 33 absorption lines, $180 \pm 1.7 \text{ km s}^{-1}$, is somewhat less than the velocities of the absorption minima in the double-peaked profiles and most of the emission lines measured at later times.

Very interestingly, in the echellette spectrum from 2008 July 6, the Ca II H and K absorption lines are apparently double, with two absorption minima (Figure 12). Evidence for the two absorption minima can still be seen in the spectrum from August 30, although the K line is much weaker. The red-shifted component has a velocity similar to that measured for the H and K lines at maximum light, while the deeper minimum has a velocity like that

Na I absorption is expected in F-type spectra. Furthermore the velocities measured for the Na I absorption lines are the same as for the other absorption lines formed in the transient’s dense wind.

of the other absorption lines and presumably originates in the same material. Although the signal-to-noise is low, evidence for the same double absorption can be seen in the profiles published by Berger et al. (2009), although they attributed the width and shape of the H and K line profiles to infall and outflow in the ejecta by analogy with a model for the ejecta for IRC +10420 (Humphreys et al. 2002). The arguments in favor of both infall and outflow for IRC +10420 however were based on the presence of inverse P Cygni profiles primarily in emission lines of Fe II, some of which showed both P Cygni and inverse P Cygni profiles. Neither are observed in the NGC 300 transient.

As mentioned in §5.3, the Na I D absorption lines transitioned from absorption to emission in about 30 days. The O I triplet at $\lambda 7774 \text{ \AA}$ is a well-known luminosity indicator for intermediate-type supergiants. Its velocities agree with those of the other absorption lines measured at the same time. It thus originates in the same material, the transient’s wind or envelope⁵. Its mean equivalent width, measured from six spectra from July 6 to August 24, is $1.62 \pm 0.08 \text{ \AA}$, corresponding to an M_V of -6.8 ± 0.2 (Osmer 1972), which coincidentally is consistent with M_V for the pre-eruption object, assuming no bolometric correction.

We have also tentatively identified Ba II in absorption at 4554 \AA and 4934 \AA in the echellette spectrum from 2008 July 6. Their respective equivalent widths are 0.5 and 0.4 \AA , with velocities of 220 and 197 km s^{-1} , slightly higher than the velocities of the other absorption lines in Table 4. Barium is an *s*-process element, so if this identification is correct, these lines may have important implications regarding the evolutionary state of the star discussed in the last section. The Ba II lines, however, are also stronger in stars of high luminosity. In the absence of an abundance analysis, these lines could be enhanced in the low-gravity environment of the wind and not necessarily be due to the *s*-process in the interior of an AGB star.

As already noted, the absorption lines weaken with time. The spectrum transitions from one with numerous absorption lines in our 2008 July echellette spectrum to one dominated by emission lines by 2008 September and later, probably due to the expansion and decreasing density of the envelope. To further illustrate this transition, we show these echellette spectra in the blue in Figure 13. None of the spectra obtained after early 2008 September show any evidence for absorption lines.

⁵The O I absorption line as well as the absorption minima in the double-peaked Ca II triplet lines are not interstellar as suggested by Berger et al. While interstellar absorption is frequently observed in the resonance transitions of Ca II (H and K lines) and Na I D, the O I and the Ca II triplet lines are not resonance lines.

6. The Transient’s Post-Eruption Outflow and Wind

The spectra of the NGC 300 OT show an object whose outflow and wind were in transition for the first 30+ days after the eruption or maximum light observed on 2008 May 15. The outflow pattern continued to develop and change for the next ~ 100 days, but after that, from approximately mid-September 2008 to our spectrum from 2009 January, the spectra are very similar and are dominated by the emission-line spectrum in the wind or ejecta. The transient thus provides an opportunity to observe a post-eruption and recovery in progress, but unfortunately, moderate- to high-resolution spectra with good signal-to-noise are lacking during the first three weeks or so. Consequently, in this section, we concentrate our discussion on the transient’s spectrum from approximately 30 days after the observed maximum.

6.1. The Eruption

Our first spectrum, from 2008 May 15, corresponds to the observed maximum light (Bond et al. 2009). The hydrogen, Ca II, and [Ca II] lines and the Ca II H and K absorption lines at that time have Doppler velocities of $400\text{--}500\text{ km s}^{-1}$ and are significantly red-shifted with respect to their velocities measured at later times (Table 4). None of the emission lines show evidence for the double-peaked profiles, which only appeared later. The Ca II triplet, however, has a very complex, broadened, and red-shifted profile, with multiple peaks perhaps indicative of multiple shells moving outwards. Berger et al.’s (2009) low-resolution spectrum from 2008 May 23 shows similar features in the Ca II triplet complex consistent with this description. The absorption lines also have higher measured Doppler velocities comparable to the emission lines (Table 4). Approximately 30 days later, mid-June 2008, the measured velocities are significantly lower, $\sim 250\text{ km s}^{-1}$, and consistent with those published by Berger et al. from the same period. High-resolution spectra published by Berger et al. show complex Ca II triplet profiles with two to three possible red-shifted components, which may be due to absorption in intervening material and infall as Berger et al. suggest. However, the deep absorption minimum in the Ca II lines at zero velocity in their Figure 14 is not interstellar.

6.2. Post-Eruption

The transition to lower velocities observed for both the emission and absorption lines is perhaps best explained as an initial eruption, followed, at approximately 30 days, by the appearance of a dense wind or envelope responsible for the absorption lines, and the possible

development of a bipolar outflow discussed below. Residual evidence for the expanding gas from the initial eruption is observed in the red-shifted absorption component of the Ca II H and K lines and possibly in the secondary emission features and broadened profiles of H α and Ca II triplet. The [Ca II] lines and the other emission lines that appear at later times must originate in the low-density gas in the surrounding ejecta. As mentioned earlier, the expected velocity of the transient is $\sim 190 \text{ km s}^{-1}$, from the NGC 300 galactic rotation curve. Based on the velocities of the emission lines, especially those that appear after 30 days, and the absorption minima in the double-peaked profiles, we suggest that the transient’s systemic velocity is $\approx 200 \text{ km s}^{-1}$. The absorption lines with a lower mean velocity of $\approx 180 \text{ km s}^{-1}$ originate in the dense slowly expanding wind.

As explained earlier, the double-peaked profiles may be attributed to a bipolar outflow, a rotating disk, or to self-absorption. We favor the outflow interpretation, for the reasons given in §5.1. Furthermore, the blue- and red-shifted primary and secondary emission components have relatively symmetric velocities, supporting an outflow model. It is not necessary to invoke a complex pattern of infall and outflow to explain the hydrogen and Ca II emission profiles observed at later times.

We use two approaches to estimate the expansion velocity. When the absorption minimum between the blue and red emission components is clearly present, the expansion velocities of the two components is simply the difference between their peak velocities and that of the absorption minimum. When there is no well-defined minimum, the estimated expansion velocity is simply half the difference in the velocities of the two maxima. The resulting expansion velocities from both methods are summarized in Table 5.

The average velocities from both the Ca II and hydrogen emission lines in the echelle spectra indicate expansion velocities for the primary wind of $\sim 70\text{--}80 \text{ km s}^{-1}$ with respect to the star, with a range from a possible high of 90 km s^{-1} for the blue component and a low of 65 km s^{-1} for the red feature. Evidence that the blue and red features may have slightly different expansion velocities comes primarily from the measurements of the Ca II triplet. The RC spectra yield slightly higher expansion velocities for the H α lines, on the order of 100 km s^{-1} . This result is not surprising at this lower resolution, given that the emission lines may be broadened by contributions from faster-moving gas. The measurements from the RC spectra also show some evidence for a higher velocity for the blue-shifted feature. Faster-moving gas is also present in the ejecta, as indicated by the width of the lines, and by the frequent presence of measurable secondary emission components, or shoulders, on the line profiles and secondary peaks in a few cases. This secondary, faster wind may also be bipolar and moving at $\approx 160 \text{ km s}^{-1}$ relative to the star.

We also note that in both the Ca II lines and H α , the blue component slowly increases

in strength relative to the red component. This observation supports our conclusion that the outflow and eruption are bipolar, with the nearer, blue-shifted lobe expanding towards us and increasing in relative intensity with respect to the receding feature. The b/r ratio is also included in Table 5.

An outflow velocity of $\sim 75 \text{ km s}^{-1}$ is typical of F-type supergiants, and is somewhat lower than the winds associated with LBVs in eruption. It is similar to the expansion velocity, $\sim 60 \text{ km s}^{-1}$, for the well-studied post-red supergiant IRC +10420 (Jones et al. 1993; Humphreys et al. 2002), measured from its double-peaked hydrogen and Ca II emission lines. Although we do not know where the emitting gas is located with respect to the star, we assume that the much stronger primary blue and red emission components originate in material closer to the star and that the outflow at 75 km s^{-1} is therefore representative of the star in its post-eruption state. The faster-moving gas at $\pm \sim 160 \text{ km s}^{-1}$ may have been produced in the initial eruption. The Doppler velocity of its red-shifted component is comparable to the higher velocities measured at maximum light.

Our model for the NGC 300 OT in post-eruption is a bipolar outflow, perhaps surrounded by low-density ejecta, with a slowly expanding dense wind or envelope producing the absorption-line spectrum, which at about 100 days after the eruption became transparent to the ionizing radiation. At later times +120 days, we see only the emission-line spectrum from the ejecta. The ionizing radiation and the increase in the UV flux could be due to the presence of a hot companion, which came apparent at later times as the dense wind expanded, or to the underlying hotter layers of the erupting star which had expelled its outer envelope.

7. On the Nature and Evolutionary State of the 2008 Optical Transient in NGC 300

With its strong, narrow hydrogen emission lines, Ca II and [Ca II] emission, and F-type supergiant absorption spectrum, the OT spectroscopically resembled the post-red supergiant IRC +10420 (Jones et al. 1993; Humphreys et al. 2002) and Var A in M33 (Humphreys et al. 2006), although these two hypergiant stars are much more luminous. Their spectroscopic similarities are telling us that the physical conditions in these stars’ winds and circumstellar ejecta are similar, not necessarily that they are the same kind of star, but like the transient, IRC +10420 and Var A have also recently experienced high-mass-loss episodes.

In other respects, the NGC 300 transient is most like SN 2008S (Prieto et al. 2008), a “supernova impostor” (Smith et al. 2008). SN 2008S was also heavily enshrouded by dust

prior to outburst, with an intrinsic luminosity of $3.5 \times 10^4 L_\odot$ from its infrared SED, implying an initial mass near $\sim 10 M_\odot$ if it was a red supergiant. It reached a visual luminosity of $M_V \simeq -14$ at maximum, increasing ~ 1000 times in luminosity during the eruption. Like the 2008 NGC 300 transient, an early spectrum showed Ca II and the rare [Ca II] lines in emission (Steele et al. 2008). SN 2010da likewise had a heavily obscured progenitor (Khan et al. 2010a; Berger & Chornock 2010). However, it is bluer and its spectrum showed significant differences. There was apparently no [Ca II] emission, but He II $\lambda 4686 \text{ \AA}$ has been identified (Elias-Rosa et al. 2010; Chornock & Berger 2010). He II emission requires a very hot source of radiation producing more than 54 eV. Binder et al. (2011) have detected an X-ray source identified with SN 2010da and suggest that it is a supergiant X-ray binary with a compact companion. SN 2010dn was spectroscopically very similar to the NGC 300 transient and SN 2008S (Smith et al. 2011). Although there is only an upper limit to its pre-outburst infrared flux (Berger 2010), its increase in apparent brightness by at least 7 magnitudes at maximum, suggest that the progenitor was very likely obscured. The progenitors of PTF 10fqz and PTF 10acbp were also not detected in the infrared, but are spectroscopically similar to these transients at maximum light (Kasliwal et al. 2010, 2011), and likewise had a large increase in apparent brightness.

The positions of the progenitors of the three transients with pre-eruption detections in the infrared are shown on an HR diagram in Figure 14. Known LBVs/S Doradus variables and several warm and cool hypergiants known for their instabilities and high-mass-loss episodes are also shown for comparison.

With the large amount of obscuring dust, the NGC 300 OT, SN 2008S, and SN 2010da must have experienced high mass-loss rates as post-main-sequence stars. At the relatively high luminosities of their progenitors, they were most likely red supergiants (RSGs), stars at the tip of the AGB, or post-AGB/RSG stars. The luminosities of the progenitors of the NGC 300 transient and SN 2008S imply relatively high initial masses, $\geq 10 M_\odot$, but they are both also close to the AGB limit. SN 2008S is just below it, and could have reached its luminosity as a somewhat lower-mass star on the AGB. Thompson et al. (2009) and Botticella et al. (2009) have suggested that these stars may represent a new class of less-luminous SNe due to electron-capture with progenitors in the mass range 8–11 M_\odot . By comparison with multi-epoch *Spitzer* IRAC observations in M33, Thompson et al. identified a group of reddened stars with similar colors that they call extreme-AGB stars that may be the progenitor class, and Khan et al. (2010b) have identified a limited population of similar self-obscured stars in four nearby galaxies, including M33, suggesting that this is a short-lived high mass loss phase.

Here we suggest that the progenitor of the NGC 300 transient, and by analogy, SN 2008S

and others described above, was an optically obscured evolved star possibly related to the OH/IR stars observed in our galaxy and the Magellanic Clouds. Given their lack of any obvious variability from multiple IRAC observations (Thompson et al. 2009), the NGC 300 transient and SN 2008S were no longer fundamental-mode pulsators, i.e., they were not Mira variables. Thus they had very likely left the region of the RSGs and AGB stars on the HR diagram and were on a blue-loop back to warmer temperatures. For that reason all three transients in Figure 14 are plotted as horizontal lines extending from the RSG/AGB region to intermediate temperatures.

Given the large amount of mass the transient must have lost as an RSG or AGB star, implied by the heavy obscuration, it must be highly evolved, possibly on a second blue loop. This suggestion is supported by the carbon-based mid-IR emission feature (Prieto et al. 2009) observed in proto-planetary nebulae and also the Ba II lines if they are due to the *s*-process. The emission feature implies carbon-rich ejecta and stars with the Ba II 4554 Å line typically show enhanced carbon features (CN, CH, and C₂). But there are no carbon features in the spectra of the wind or envelope, and instead the spectrum has strong O I absorption and emission lines.

The luminosity of the NGC 300 OT progenitor places it slightly above the AGB limit and implies an initial mass of 10–15 M_{\odot} if it was a true supergiant, and Gogarten et al. (2009) estimated a mass range of 13–17 M_{\odot} based on the CMD of the associated stellar population. Our inspection of the transient’s immediate environment was inconclusive for the mass of the progenitor. The mid-IR emission feature, however, supports a post-AGB origin for the progenitor and by implication a lower mass, $<10 M_{\odot}$. These results are not necessarily inconsistent. Stars with initial masses in the 5–9 M_{\odot} range, when at the tip of the AGB, can reach the luminosities of the NGC 300 OT and SN 2008S progenitors. Thus both objects could have originated from stars with initial masses in this range, for which the later stages of evolution are somewhat uncertain. Furthermore there is no reason why a true supergiant could not pass through the RSG region more than once. Evolutionary tracks for stars in the 9–12 M_{\odot} range show a second approach to the RSG region Maeder & Meynet (2000).

The presence of Ca II and [Ca II] emission, observed in the winds of the F-type hypergiants, also suggests that the progenitor was not as hot as a B-type supergiant, as in the case of LBV eruptions, but may have been somewhat cooler, more likely an intermediate-temperature star. The implication that the underlying star was also somewhat warmer than an RSG or AGB star is supported by its bipolar outflow with speeds of $\sim 75 - 100 \text{ km s}^{-1}$ near the star and somewhat faster-moving ejecta at $\approx 160 \text{ km s}^{-1}$, probably further from the star. These velocities are significantly higher than the winds associated with RSGs,

AGB stars, and the OH/IR stars ($\sim 15\text{--}25 \text{ km s}^{-1}$ for the AGB stars, and up to 40 km s^{-1} for the OH/IR supergiants). The [Ca II] emission, however, originates in slower-moving, lower-density gas, possibly a remnant from the progenitor’s earlier state, as an AGB star or RSG.

The transient was thus most likely an evolved intermediate-mass star in transition to warmer temperatures that had recently experienced high mass loss. Having already shed a lot of mass, these stars are at or near the Eddington-limit for their luminosities. In their post-RSG or post-AGB evolution, they will encounter a temperature regime (6000–9000 K) of increased dynamical instability (de Jager 1998) driven by the increasing opacity in combination with increasing rotation and pulsation. For example, the less-luminous LBVs (Humphreys & Davidson 1994) are generally considered to be post-red supergiants. With their reduced mass they are much closer to the Eddington limit for their luminosities and are therefore more subject to radiation pressure and other instabilities. Although it is not known if these instabilities can lead to a major eruption, the most famous example may be the progenitor of SN 1987A. Its interlocking bipolar loops and equatorial ring are evidence for high-mass-loss events prior to the terminal explosion. Although the rings have been attributed to the RSG stage, they closely resemble the ejecta around many LBVs (Humphreys & Davidson 1994), and Smith (2007) has emphasized their resemblance to the ejecta associated with the LBV candidate HD 168625. However, the transient’s bipolar eruption may be an equally likely model for SN 1987A’s pre-supernova ejecta and for high-mass-loss episodes for post-RSG stars evolving to the LBV stage as well as post-AGBs/proto-planetary nebulae (see Soker & Kashi 2011). In this case, the onset of the ionizing radiation and increased UV flux required for the observed transition to the emission line spectrum may be due to an underlying hotter zone, revealed when the expanded cool, dense wind or false photosphere dissipated.

The NGC 300 2008 OT and related objects like SN 2008S are not classical or normal LBVs/S Dor variables. Although they have experienced a “giant eruption,” increasing their total luminosity by 100 to 1000 times, they are also not examples of giant-eruption LBVs (Humphreys & Davidson 1994). The progenitors are apparently less luminous, intermediate-mass stars on a blue loop that have previously shed a lot of mass. Although the origin of the NGC 300 transient’s eruption is not known, it briefly increased its total luminosity by about 250 times and released 10^{47} ergs. The eruption produced a cool dense envelope and a two-component bipolar outflow. It may have been some type of yet unexplained failed supernova or a sub-photospheric eruption expelling up to $1 M_{\odot}$ in transit to a warmer state.

The authors gratefully acknowledge the support of the SMARTS consortium to obtain the multi-wavelength photometry and the RC series of spectra. We thank the European

Southern Observatory for Director’s Discretionary Time for the near-infrared spectra in 2009 July, VLT/UT1/ISAAC proposal: 283.D-5019(A,B,C,D). We also thank Elena Sabbi for her assistance with analysis of the CMD and determining the TRGB distance to NGC 300, and G. Pietrzyński and Julio Chanamé who obtained the MagE spectra on 2008 July 6 and 2009 June 5, respectively. Prieto acknowledges support from NASA through Hubble Fellowship grant HF-51261.01-A awarded by STScI, which is operated by AURA, Inc. for NASA, under contract NAS 5-2655.

Appendix Table A1 and A2 Table A1 (Photometry) and Table A2 Journal of Spectroscopic Observations will be in the electronic version.

REFERENCES

- Anderson, J., et al. 2008, *AJ*, 135, 2055
- Auer, L. H., & Van Blerkom, D. 1972, *ApJ*, 178, 175
- Bedin, L. R., Cassisi, S., Castelli, F., Piotto, G., Anderson, J., Salaris, M., Momany, Y., & Pietrinferni, A. 2005, *MNRAS*, 357, 1038
- Berger, E., et al. 2009, *ApJ*, 699, 1850
- Berger, E. 2010, *The Astronomer’s Telegram*, 2655
- Berger, E. & Chornock, R. 2010, *The Astronomer’s Telegram*, 2638
- Binder, B., Williams, B. F., Kong, A. K. H., Gaetz, T. J., Plucinsky, P. P., Dalcanton, J. J., & Weisz, D. R. 2011, arXiv:1105.2317v1
- Bond, H. E., et al. 2003, *Nature*, 422, 405
- Bond, H. E., & Siegel, M. H. 2006, *ApJ*, 131, 984
- Bond, H. E., Bedin, L. R., Bonanos, A. Z., Humphreys, R. M., Monard, L. A. G. B., Prieto, J. L., & Walter, F. M. 2009, *ApJ*, 695, L154
- Bond, H. E. 2010, *The Astronomer’s Telegram*, 2640
- Bond, H. E. 2011, *ApJ*, 737, 17
- Botticella, M. T., et al. 2009, *MNRAS*, 398, 1041
- Bowen, I. S. 1947, *PASP*, 59, 196

- Bresolin, F., Pietrzyński, G., Gieren, W., & Kudritzki, R.-P. 2005, *ApJ*, 634, 1020
- Chornock, R. & Berger, E. 2010, *The Astronomer's Telegram*, 2637
- Davidson, K. 1987, *ApJ*, 317, 760
- de Jager, C. 1998, *A & A Rev.*, 325, 714
- DePoy, D., et al. 2003, *SPIE*, 4841, 827
- Elias-Rosa, N., Mauerhan, J. C. & Van Dyk, S. D. 2010, *The Astronomer's Telegram*, 2636
- Gieren, W., et al. 2005, *ApJ*, 628, 695
- Gogarten, S. M., Dalcanton, J. J., Murphy, J. W., Williams, B. F., Gilbert, K. & Dolphin, A. 2009, *ApJ*, 703, 300
- Gogarten, S. M., et al. 2010, *ApJ*, 712, 858
- Grandi, S. A. 1980, *ApJ*, 238, 10
- Hillier, D. J. 1991, *A&A*, 247, 455
- Humphreys, R.M. & Davidson, K. 1994, *PASP*, 106, 1025
- Humphreys, R.M., Davidson, K., & Smith, N. 1999, *PASP*, 111, 1124
- Humphreys, R.M., Davidson, K., & Smith, N. 2002, *AJ*, 124, 1026
- Humphreys, R. M., et al. 2006, *AJ*, 131, 2105
- Jones, T. J., Humphreys, R. M., Gehrz, R. D. et al 1993, *ApJ*, 411, 323
- Kasliwal, M. M., et al. 2010, *The Astronomer's Telegram*, 3094
- Kasliwal, M. M., et al. 2011, *ApJ*, 730, 134
- Kelly, J., Cenko, S. B., Li, W., & Filippenko, A. V, 2011, *CBET* 2754
- Kelson, D. D. 2003, *PASP*, 115, 688
- Khan, R., Stanek, K. Z., Kochanek, C. S., & Thompson, T. A., 2010a, *The Astronomer's Telegram*, 2632
- Khan, R., Stanek, K. Z., Prieto, J. L., Kochanek, C. S., Thompson, T. A., & Beacom, J. F. 2010b, *ApJ*, 715, 1094

- Kulkarni, S. R. et al. 2007, *Nature*, 447, 458
- Madore, B.F., & Freedman, W.L. 1995, *AJ*, 109, 1645
- Maeder, A. & Meynet, G. 2000, *A&A*, 361, 101
- Marcelin, M., Boulesteix, J., & Georgelin, Y. P. 1985, *A&A*, 151, 144
- Marshall, J. L. et al. 2008, *SPIE*, 7014, 169
- Martini, P., et al. 1999, *AJ*, 118, 1034
- Mason, E., Diaz, M., Williams, R. E., Preston, G. & Bensby, T. 2010, *A&A*, 515, 108
- Monard, L. A. G. B., 2010, *CBET*, 2289
- Osmer, P. S., 1972, *ApJS*, 24, 247
- Prieto, J. L., et al. 2008, *ApJ.*, 681, L9
- Prieto, J.L., 2008, *The Astronomer’s Telegram*, 1550, 1
- Prieto, J. L., Sellgren, K., Thompson, T. A., & Kochanek, C. S. 2009, *ApJ*, 705, 1425
- Rau, A., Kulkarni, S. R., Ofek, E. O. & Yan, L. 2007, *ApJ*, 659 1536
- Rizzi, L., Bresolin, F., Kudritzki, R.-P., Gieren, W., & Pietrzyński, G. 2006, *ApJ*, 638, 766
- Sakai, S., Madore, B.F., & Freedman, W.L. 1996, *ApJ*, 461, 713
- Sirianni, M., et al. 2005, *PASP*, 117, 1049
- Smith, N. 2007, *AJ.*, 133, 1034
- Smith, N., et al. 2009, *ApJ*, 697, 49
- Smith, N., Li, W., Silverman, J. M., Ganeshalingam, M., & Filippenko, A. V. 2011, *MNRAS*,
- Soker, N & Kashi, A., 2011, *arXiv:1108.2257*
- Steele, T. N. et al. 2008, *CBET*, 1275
- Thompson, T., Prieto, J. L., Stanek, K. Z., Kistler, M. D., Beacom, J. F. & Kochanek, C. S. 2009, *ApJ*, 705, 1364
- Tylenda, R. & Soker, N. 2006, *A&A*, 451, 223

Tylenda, R., et al., 2011, A&A, 528, 114

Van Dyk, S. D., et al. 2000, PASP, 112, 1532

This preprint was prepared with the AAS L^AT_EX macros v5.2.

Table 1. RC Spectrograph Gratings

Grating	Wavelength Range Å	Resolution Å
9	4770-7180	8.6
13	3150-9350	17.2
26	3660-5440	4.3
47	5650-6970	3.1
58	6000-9000	6.5

Table 2. Measured Velocities for the Ca II Triplet Emission Lines from the Echellette Spectra

U.T. Date 2008	Line Id. Å	Blue Pk. km s ⁻¹	Abs. Min. km s ⁻¹	Red Pk. km s ⁻¹	Comment
Jul 06	λ8498 primary	120	198	266	...
	... secondary	10	...	336	^a
	λ8542	67	189	304	asymmetric to red ^b
	λ8662 primary	97	190	294	blue & red peaks appear double ^c
	... secondary	61	...	378	...
Aug 30	λ8498	117	...	265 ^d	line appears single ^d
	λ8542 primary	107	188	251	...
	... secondary	35	...	400	^e
	λ8662 primary	105	201	254	...
	... secondary	49	^f
Sep 01	λ8498	123	...	248	^g
	λ8542 primary	96	193	242	...
	... secondary	31	...	349	^h
	λ8662 primary	119	183	249	...
	... secondary	69	...	383	^e

^aAn emission shoulder is present on the blue and red sides, respectively of the two emission peaks.

^bThe red component is asymmetric with a wing extending to 8570 Å.

^cThe blue and red-shifted components each have two approximately equal peaks. The red component also has a prominent redward extending wing.

^dThe line appears single with a small shoulder on the red side. There is no absorption minimum.

^eThe blue side of the profile has a small secondary peak and the red component has a red shoulder.

^fThe blue side of the profile has a small secondary peak. There is no shoulder on the red component.

^gThe line appears single with a prominent shoulder on the red side and small shoulder or bump on the blue side with a velocity of -8 km s⁻¹.

^hThe blue side of the profile has a small secondary peak, and the red side has a shoulder.

Table 3. Measured Velocities for the Double–Peaked Hydrogen Emission Lines

U.T. Date	Line Id.	Blue Pk. km s ⁻¹	Abs. Min . km s ⁻¹	Red Pk. km s ⁻¹	Comment
Echellette and ISAAC Spectra					
2008 Jul 06	H α primary	141	215	297	...
	... secondary	18	...	433	^a
	H β	128	...	370	^b
2008 Aug 30	H α primary	137	212	265	^c
	... secondary	446	red shoulder
	H β	113	207	262	...
2008 Sep 01	H α primary	126	192	258	...
	H β	156	236	283	...
2009 Jun 05	H α primary	112	188	239	...
	... secondary	24
2009 Jul 19 – 23	Br γ	86	184	258	VLT/ISAAC
H α – RC Spectra with grating #47, all 2008					
Jun 21	...	107	205	286	^d
Aug 25	...	78	216	293	...
Sep 10	...	94	207	293	...
Sep 13	...	90	...	318	^e
Sep 16	...	107	241:	301	...
Sep 27	...	112	...	323	^e
Oct 13	...	104	...	358	^e
Nov 03	...	112	...	279	^e
Nov 09	...	140	...	282	^e

^aThe blue and red peaks each have a small shoulder.

^bRed shoulder; no absorption minimum.

^cThe blue-shifted emission profile is very broad, this velocity is for the peak.

^dTwo small maxima at the top of an otherwise single profile.

^eNo measurable absorption minimum

Table 4. Radial Velocity Summary for the Emission and Absorption Lines

Identification	U.T. Date 2008	Velocity km s ⁻¹	Comment
Emission Lines			
H α	15 May	395	FWHM 1050 km s ⁻¹ , Gr #13
	20 Jun	201	FWHM 981 km s ⁻¹ , Gr #13
H (Paschen lines) [Ca II] ($\lambda\lambda$ 7291,7323)	30 Aug – 01 Sep	155 \pm 8	6 lines, echellette
	15 May	478, 363	Gr # 13
	20 Jun	250, 238	Gr # 13
	06 Jul	208, 229	echellette
	30 Aug – 01 Sep	202, 222	echellette
He I (λ 5876)	06 Jul – 19 Dec	208, 227	mean, 7 obs., Gr #58
	20 Jun	147:	Gr #13
	06 Jul	155	echellette
O I (λ 8446)	30 Aug – 01 Sep	155	echellette
	06 Jul	215	echellette
	07 Aug	218	Gr #58
	24 Aug	126	Gr #58
	30 Aug – 01 Sep	153	echellette
	21 Sep	108	Gr #58
	07 Nov	109	Gr #58
[O I] ($\lambda\lambda$ 6300,6363)	06 Jul	197,—	echellette
	30 Aug – 01 Sep	205,204	echellette
Na I D ($\lambda\lambda$ 5890,5896)	24 Aug	210,245	Gr #47
	30Aug-01Sep	252,255	echellette
Fe II (7 lines)	06 Jul	230 \pm 10	echellette
" (12 lines)	30Aug-01Sep	210 \pm 4	echellette
[Fe II] (2 lines)	06 jul	205 \pm 3	echellette
" (14 lines)	30Aug-01Sep	207 \pm 6	echellette
Absorption Lines			
Ca II H	15 May	409	Gr #13
	06 Jul	191,342	echellette, double abs.
	30 Aug – 01 Sep	182	echellette
Ca II K	15 May	453	Gr #13
	06 Jul	181,402	echellette, double abs.
	30 Aug – 01 Sep	195,432	echellette, double abs.
Na I D (5890,5896)	20 Jun	184	blend, #13
	06 Jul	176,175	echellette
	30 Aug – 01 Sep	177,184	echellette

Table 4—Continued

Identification	U.T. Date 2008	Velocity km s ⁻¹	Comment
O I ($\lambda 7774$)	06 Jul	140:	Gr #58
	06 Jul	183	echellette
	01 Aug	208	Gr #58
	07 Aug	218	Gr #58
	30 Aug – 01 Sep	178	echellette
Ba II: ($\lambda 4554, 4934$)	06 Jul	220, 197	echellette
Other Absorption lines (Sr II, Ca I, Mn I, Ti II, V II)	06 Jul	179 ± 2.2	echellette, 24 lines

Table 5. Expansion Velocities from the Double Ca II and Hydrogen Emission Lines

U.T. Date	Line Id.(Å)	Blue Pk. km s ⁻¹	Red Pk. km s ⁻¹	Peak to Peak km s ⁻¹	b/r
Ca II Triplet					
2008 Jul 06	λ8498 primary	-78	68	73	1.13
	... secondary	163	...
	λ8542	-122	115	118	1.17
	λ8662 primary	-93	104	99	1.27
2008 Aug 30	... secondary	nodata	...	160	...
	λ8498	74	...
	λ8542 primary	-81	63	72	1.40
	... secondary	183	...
2008 Sep 01	λ8662 primary	-96	53	75	1.46
	λ8498	63	...
	λ8542 primary	-97	49	73	1.38
	... secondary	159	...
Avg	λ8662 primary	-64	66	65	1.47
	... secondary	157	...
	primary	-90 ± 6.4	74 ± 8.9	79 ± 5.6	
	secondary	164 ± 4.2	
Hydrogen – Echellette and ISAAC					
2008 Jul 06	Hα primary	-74	72	78	1.06
	... secondary	207	...
	Hβ	121	1.38
2008 Aug 30	Hα primary	-75	53	64	1.32
	Hβ	-94	55	75	1.88
2008 Sep 01	Hα primary	-66	66	66	1.36
	Hβ	-80	47	64	1.83
2009 Jun 05	Hα primary	-76	51	64	1.5
2009 Jul 19-23	Brγ	-93	74	86	...
Avg	Hα primary	-73 ± 2.0	60 ± 4.7	68 ± 2.9	
	Hβ	-87 ± 7	51 ± 4	70 ± 5	
Hα – RC Spectra (grating #47), all 2008					
Jun 21	...	-98	81	90	1.03
Aug 25	...	-138	77	108	...
Sep 10	...	-113	86	100	1.24
Sep 13	114	...
Sep 16	...	-134:	60:	97	1.37
Sep 27	106	...

Table 5—Continued

U.T. Date	Line Id.(Å)	Blue Pk. km s ⁻¹	Red Pk. km s ⁻¹	Peak to Peak km s ⁻¹	b/r
Oct 13	127	1.42
Nov 03	84	...
Nov 09	71	1.42
Avg	...	-121 ± 8.1	76 ± 4.9	100 ± 5.2	...

Table A1. SMARTS 1.3-m ANDICAM Photometry of NGC 300 OT2008-1

HJD– 2400000	Elapsed days	<i>B</i>	<i>V</i>	<i>R</i>	<i>I</i>	<i>J</i>	<i>H</i>	<i>K</i>
54600.646	0.000	14.181
54601.642	0.996	14.231
54602.936	2.290	15.495	14.687	14.211	13.714	13.052	12.501	11.435
54606.910	6.264	15.525	14.707	14.251	13.804	13.048	12.675	11.694
54607.939	7.293	15.535	14.707	14.261	13.834	13.065	12.585	11.643
54608.904	8.258	15.595	14.747	14.271	13.814	13.042	12.544	11.717
54609.902	9.256	15.655	14.767	14.291	13.814	13.109	12.622	11.675
54610.873	10.227	15.615	14.787	14.271	13.824	13.093	12.657	11.470
54611.886	11.240	15.655	14.777	14.291	13.854	13.062	12.563	11.781
54615.934	15.288	15.745	14.867	14.331	13.854	13.043	12.565	11.708
54623.911	23.265	15.915	14.977	14.381	13.874	13.027	12.641	11.607
54624.879	24.233	15.965	14.967	14.391	13.894	13.102	12.579	11.659
54626.877	26.231	15.985	15.007	14.411	13.914	13.106	12.640	11.676
54627.876	27.230	15.995	15.007	14.411	13.884	13.093	12.578	11.759
54628.899	28.253	16.015	15.027	14.411	13.894	13.017	12.567	11.677
54629.835	29.189	16.055	15.027	14.441	13.914	13.117	12.551	11.911
54630.878	30.232	16.075	15.067	14.431	13.914	13.081	12.639	11.887
54631.861	31.215	16.095	15.067	14.431	13.924	13.143	12.673	11.741
54633.888	33.242	16.115	15.097	14.451	13.914	13.043	12.658	11.477
54634.863	34.217	16.195	15.127	14.471	13.934	13.069	12.660	11.625
54637.847	37.201	16.215	15.167	14.511	13.974	13.167	12.729	11.592
54638.907	38.261	16.295	15.207	14.541	13.994	13.140	12.646	11.896
54639.891	39.245	16.335	15.207	14.591	14.034	13.315	12.653	...
54640.842	40.196	16.335	15.277	14.551	14.014	13.189	12.627	11.847
54641.878	41.232	16.375	15.267	14.611	14.064	13.202	12.688	11.664
54642.878	42.232	16.395	15.337	14.621	14.094
54643.868	43.221	16.415	15.347	14.671	14.084	13.193	12.724	11.964
54644.876	44.230	16.455	15.357	14.661	14.134	13.167	12.797	11.960
54645.882	45.236	16.495	15.387	14.691	14.134	13.188	12.787	11.999
54646.799	46.153	16.505	15.427
54647.894	47.248	16.575	15.447	14.751	14.174	13.231	12.802	...
54648.844	48.198	16.595	15.487	14.781	14.214	13.398	12.964	12.187
54649.903	49.257	16.625	15.517	14.801	14.234	13.358	12.888	12.089
54650.839	50.193	16.675	15.547	14.841	14.244	13.430	12.941	12.036
54651.837	51.191	16.705	15.597	14.861	14.284	13.350	12.914	11.981
54652.859	52.213	16.745	15.627	14.891	14.314	13.389	12.929	12.032

Table A1—Continued

HJD– 2400000	Elapsed days	<i>B</i>	<i>V</i>	<i>R</i>	<i>I</i>	<i>J</i>	<i>H</i>	<i>K</i>
54653.849	53.203	16.725	15.657	14.911	14.334	12.225
54654.887	54.240	16.845	15.697	14.951	14.374	13.504	12.907	...
54655.892	55.246	16.875	15.747	14.991	14.404	13.441	12.944	12.237
54657.851	57.205	16.955	15.777	15.031	14.474	13.474	12.976	11.971
54658.887	58.241	16.935	15.867	15.071	14.474
54660.879	60.233	17.095	15.977	15.181	14.534	13.545	13.141	12.151
54661.883	61.237	17.115	15.987	15.201	14.594
54662.898	62.252	17.185	16.037	15.231	14.614	13.598	13.060	12.290
54663.875	63.229	17.235	16.067	15.281	14.654	13.556	13.019	12.253
54664.891	64.245	17.295	16.147	15.311	14.674	13.653	13.081	12.295
54665.885	65.239	17.335	16.167	15.331	14.714	13.614	13.013	12.185
54666.804	66.158	17.355	16.207	15.381	14.764	13.698	13.175	11.988
54671.794	71.148	17.655	16.477	15.601	14.904	13.722	13.116	12.237
54672.880	72.234	17.705	16.517	15.631	14.954	13.788	13.055	12.342
54674.824	74.178	17.765	16.607	15.681	14.994	13.870	13.188	12.500
54678.801	78.155	18.015	16.857	15.871	15.154	13.897	13.205	12.378
54681.878	81.232	18.245	17.037	16.011	15.254	13.970	13.249	12.417
54682.809	82.163	18.255	17.067	16.051	15.314	13.974	13.214	12.281
54683.813	83.167	18.325	17.137	16.091	15.334	14.027	13.318	12.230
54684.773	84.127	18.385	17.207	16.151	15.384	14.002	13.305	12.232
54685.778	85.132	18.455	17.277	16.181	15.394	14.082	13.297	12.305
54686.804	86.158	18.535	17.317	16.241	15.444	14.060	13.344	12.528
54687.779	87.133	18.585	17.377	16.271	15.494	14.084	13.238	12.592
54688.865	88.219	18.625	17.447	16.341	15.534	14.112	13.361	12.624
54690.829	90.183	18.775	17.587	16.431	15.634	14.070	13.297	12.440
54698.787	98.141	19.285	18.167	16.871	16.014	14.340	13.495	12.628
54701.761	101.115	19.515	18.367	17.041	16.184	14.457	13.475	12.796
54704.786	104.140	19.695	18.637	17.211	16.354	14.506	13.594	12.661
54708.767	108.121	19.955	18.987	17.461	16.634	14.712	13.726	12.649
54715.779	115.133	20.345	19.447	17.811	17.054	14.886	13.915	12.760
54717.746	117.100	20.425	19.497	17.901	17.154	15.024	14.031	12.959
54721.762	121.116	18.001	17.294	14.994	14.092	12.971
54724.805	124.159	20.855	19.867	18.051	17.354	15.365	14.246	13.014
54728.708	128.062	...	19.837	18.101	17.494	15.333	14.224	13.102
54732.732	132.086	21.015	19.927	18.211	17.634	15.354	14.288	13.115
54735.744	135.098	18.231	17.674	15.582	14.429	13.299

Table A1—Continued

HJD– 2400000	Elapsed days	<i>B</i>	<i>V</i>	<i>R</i>	<i>I</i>	<i>J</i>	<i>H</i>	<i>K</i>
54738.711	138.065	21.075	20.157	18.331	17.754	15.784	14.596	13.187
54739.748	139.102	21.075	20.147	18.311	17.774	15.742	14.572	13.302
54744.712	144.066	21.185	20.257	18.421	17.844	15.777	14.569	13.304
54749.713	149.067	21.195	20.187	18.451	17.954	16.032	14.765	13.255
54754.711	154.065	21.155	20.327	18.531	18.054	16.131	14.812	13.361
54760.708	160.062	21.345	20.487	18.571	18.114	16.282	14.832	13.413
54766.725	166.079	21.565	20.547	18.681	18.214	16.356	14.999	13.457
54772.674	172.028	21.525	20.727	18.711	18.304	16.297	15.104	13.561
54778.644	177.998	21.625	20.787	18.791	18.394	16.496	15.067	13.570
54784.671	184.025	21.725	20.967	18.821	18.524	16.612	15.181	13.565
54794.651	194.005	21.795	20.957	18.941	18.574	16.681	15.322	13.593
54801.645	200.999	22.095	21.127	18.941	18.614	16.861	15.370	13.709
54807.643	206.997	18.991	18.674	...	15.312	13.808
54817.602	216.956	...	21.147	19.021	18.814	...	15.499	13.754
54827.608	226.962	...	21.367	19.171	18.874
54839.608	238.962	19.231	18.994
54845.543	244.897	19.371
54847.563	246.917	...	21.687
54848.546	247.900	19.331
54849.535	248.889	19.174
54851.557	250.911	...	21.717
54852.540	251.894	19.371
54853.534	252.888	19.144
54855.554	254.908	...	21.767
54857.530	256.884	19.234
54861.529	260.883	19.294
54872.532	271.886	19.521
54873.529	272.883	19.324
54962.912	362.266	19.675
54964.920	364.274	21.281	16.233	...
54965.887	365.241	14.389
54975.905	375.259	19.240	16.386	14.157
54982.905	382.259	20.536	16.642	14.445
54995.883	395.237	20.545	16.998	14.485
55005.908	405.262	22.191	22.544	20.834	16.820	14.473
55014.914	414.268	20.493	17.194	14.394

Table A1—Continued

HJD– 2400000	Elapsed days	<i>B</i>	<i>V</i>	<i>R</i>	<i>I</i>	<i>J</i>	<i>H</i>	<i>K</i>
55036.822	436.176	20.760

Note. — First two lines are Bronberg discovery observations, taken to be *R* magnitudes. All other data from 1.3-m ANDICAM frames. Typical errors are ± 0.02 – 0.04 mag until end of 2008 (HJD \simeq 54830), increasing thereafter to approximately ± 0.1 – 0.2 mag as the transient faded.

Table A2. Journal of Spectroscopic Observations

Date (UT)	Spec/Grating	Integration (sec)	Comment
2008 May 15	RC 13	3x 300	
2008 May 16	RC 26	3x 600	no signal
2008 May 17	RC 9	3x 600	
2008 Jun 20	RC 13	3x 600	
2008 Jun 21	RC 47	3x 600	
2008 Jun 22	RC 26	3x 900	only H-beta detected
2008 Jul 06	RC 58	3x 800	
2008 Jul 06	MagE/echellette	2x 800	
2008 Jul 08	RC 58	3x 600	
2008 Jul 18	RC 13	3x 600	
2008 Aug 01	RC 58	3x 600	
2008 Aug 06	RC 26	3x1200	
2008 Aug 07	RC 58	3x 600	
2008 Aug 23	RC 13	3x 900	
2008 Aug 24	RC 58	3x1000	
2008 Aug 25	RC 47	3x1100	
2008 Aug 30	MagE/echellette	900	
2008 Sep 01	MagE/echellette	900	
2008 Sep 08	RC 13	3x1000	
2008 Sep 10	RC 47	3x1200	
2008 Sep 13	RC 47	3x1200	
2008 Sep 16	RC 47	3x1200	
2008 Sep 21	RC 58	3x 600	
2008 Sep 27	RC 47	3x1200	
2008 Sep 28	RC 26	3x1200	
2008 Oct 01	RC 13	3x 900	
2008 Oct 03	RC 47	3x1200	
2008 Oct 12	RC 47	3x1200	
2008 Oct 13	RC 13	3x1200	
2008 Nov 03	RC 47	3x1200	
2008 Nov 04	RC 13	3x1200	
2008 Nov 07	RC 58	3x 900	
2008 Nov 09	RC 47	3x1200	
2008 Nov 13	RC 13	3x1200	
2008 Dec 01	RC 47	3x1200	
2008 Dec 06	RC 13	3x1100	
2008 Dec 19	RC 58	3x 900	

Table A2—Continued

Date (UT)	Spec/Grating	Integration (sec)	Comment
2008 Dec 30	RC 13	3x1200	
2009 Jan 16	RC 47	3x1200	
2009 Jun 05	MagE/echellette	3000	
2009 Jul 19 – 23	ISAAC		1.65 μ m, 2.2 μ m, 3.55 μ m

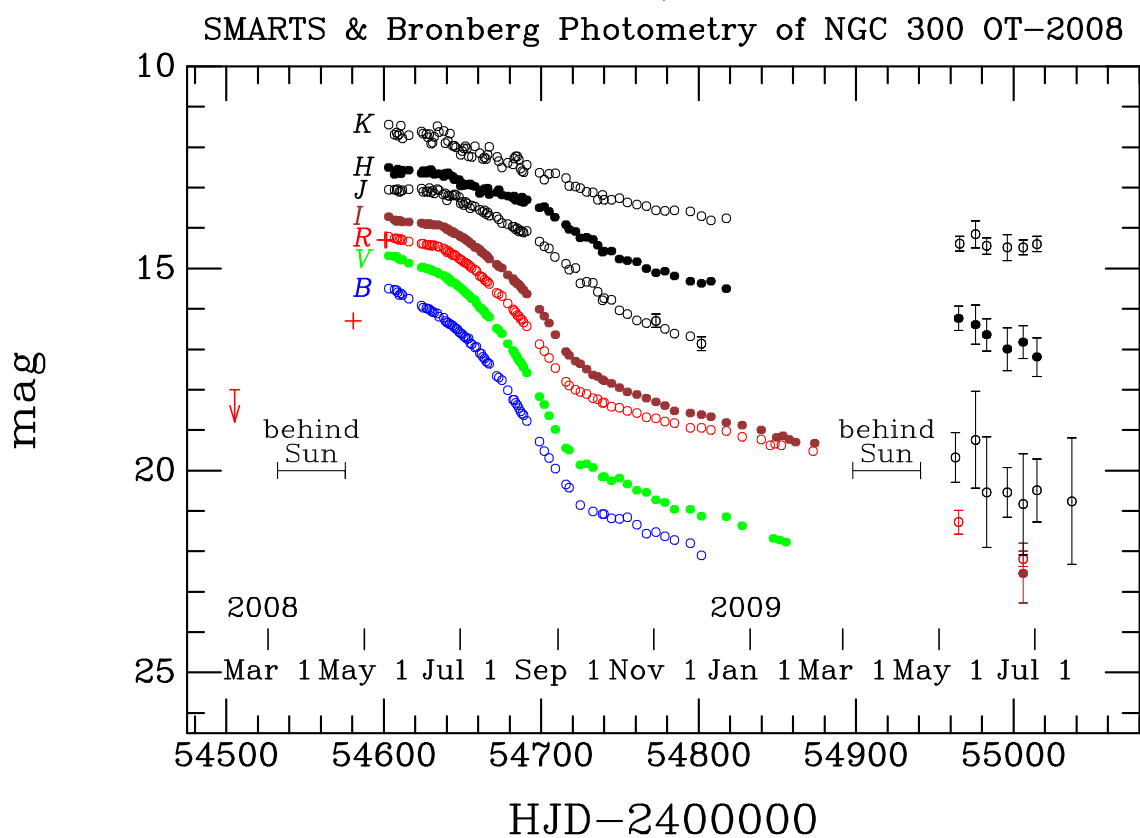


Fig. 1.— *BVRIJHK* light curve of NGC 300 OT 2008. SMARTS 1.3-m data are shown as open and filled circles; error bars are plotted only when larger than the plotting symbols. Bronberg discovery observations and the pre-discovery detection are shown as crosses (these broad-band magnitudes are close to Landolt *R*), and the downward arrow on the left shows the Bronberg upper limit in 2008 February. To appear in color in the electronic edition.

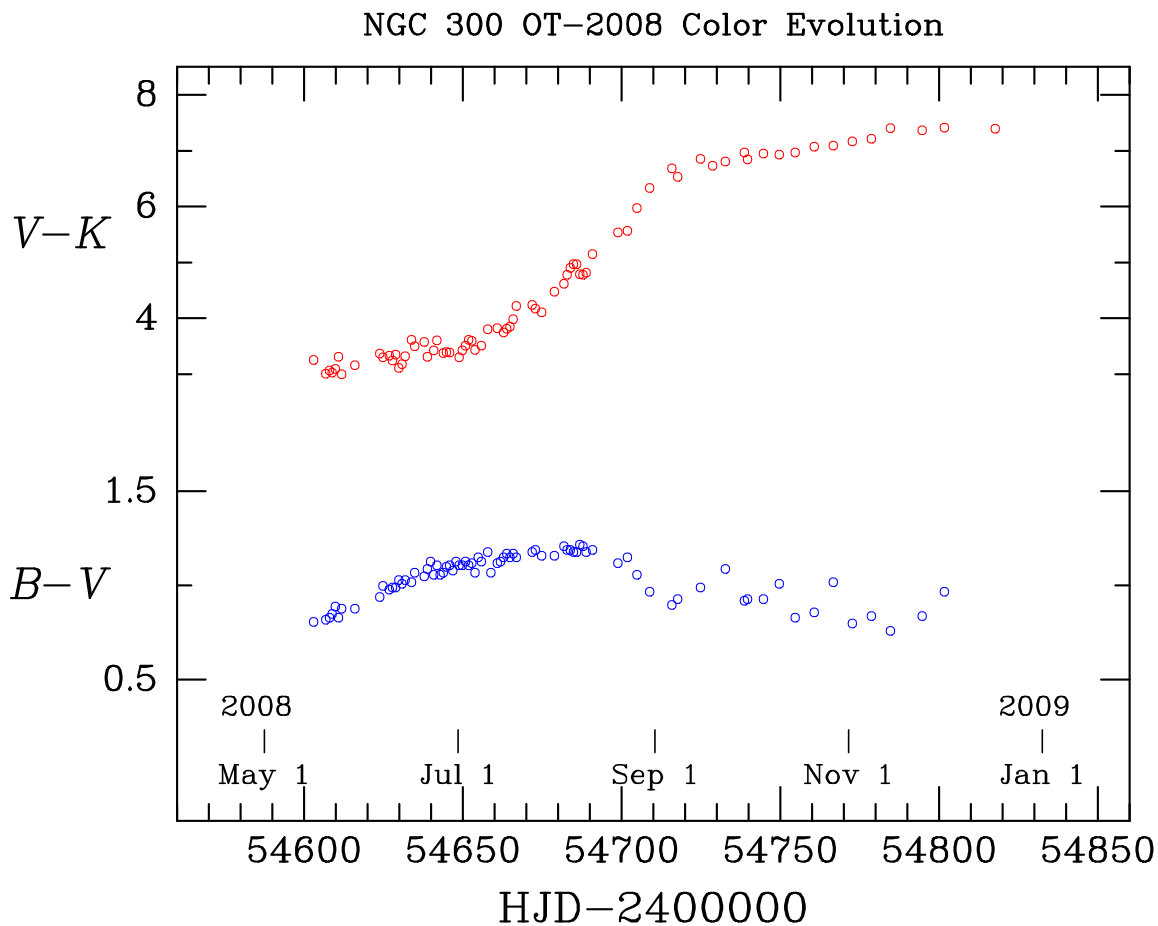


Fig. 2.— The $B - V$ and $V - K$ colors of NGC 300 OT 2008 vs. time. The $V - K$ color (top points) became dramatically redder as the outburst proceeded, evolving from 3.1 in mid-May 2008 to ~ 7.4 at the end of our coverage. The $V - K$ slope changed markedly in 2008 September, due to the change in slope of V vs. time. As discussed in the text (§3), $B - V$ also became progressively redder with time, until 2008 August. It then became *bluer* with time until the end of our coverage. To appear in color in the electronic edition.

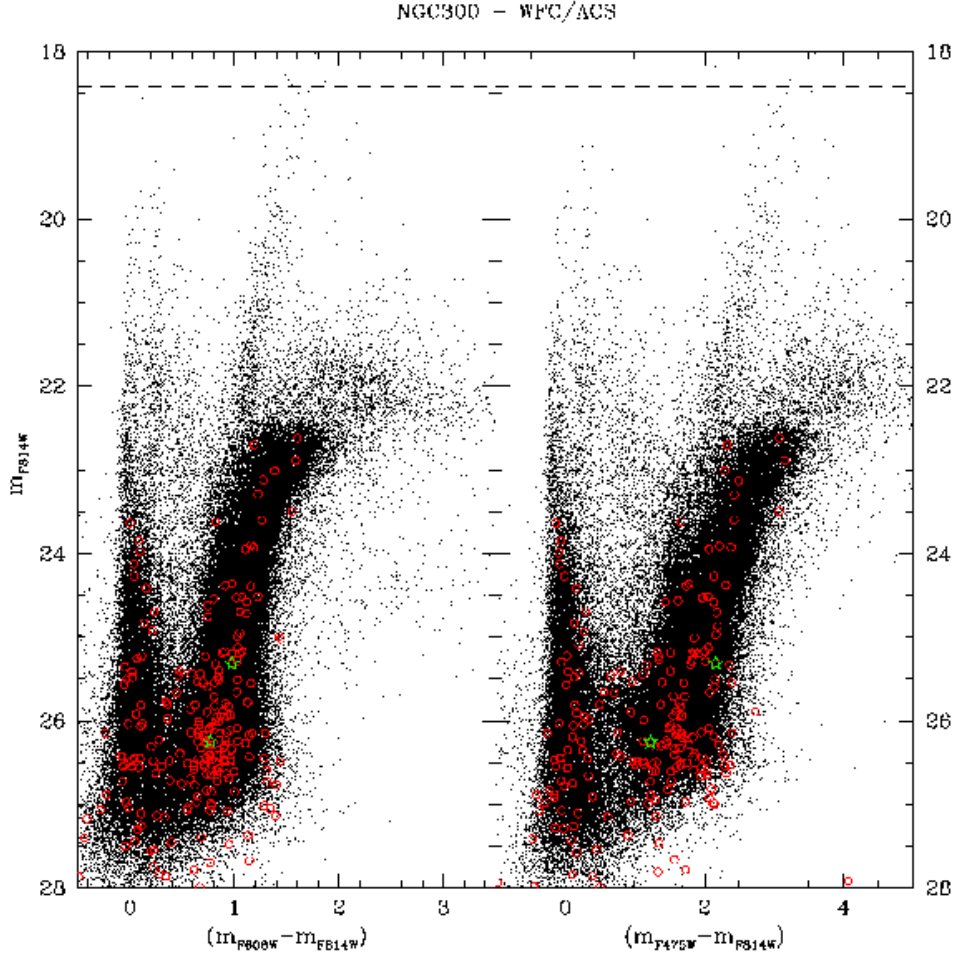


Fig. 3.— Deep CMDs derived from the archival *HST*/ACS and WFC images, as described in the text. The left frame shows I vs. $V - I$, and the right frame shows I vs. $B - I$. Black dots show all point sources with reliable photometry. The red circles mark stars within a radius of $2''.5$ (23 pc) from the NGC 300 OT. The two green stars are the two only stars lying within $0''.25$ (2.3 pc) from the site of the OT, but well outside the astrometric error box.

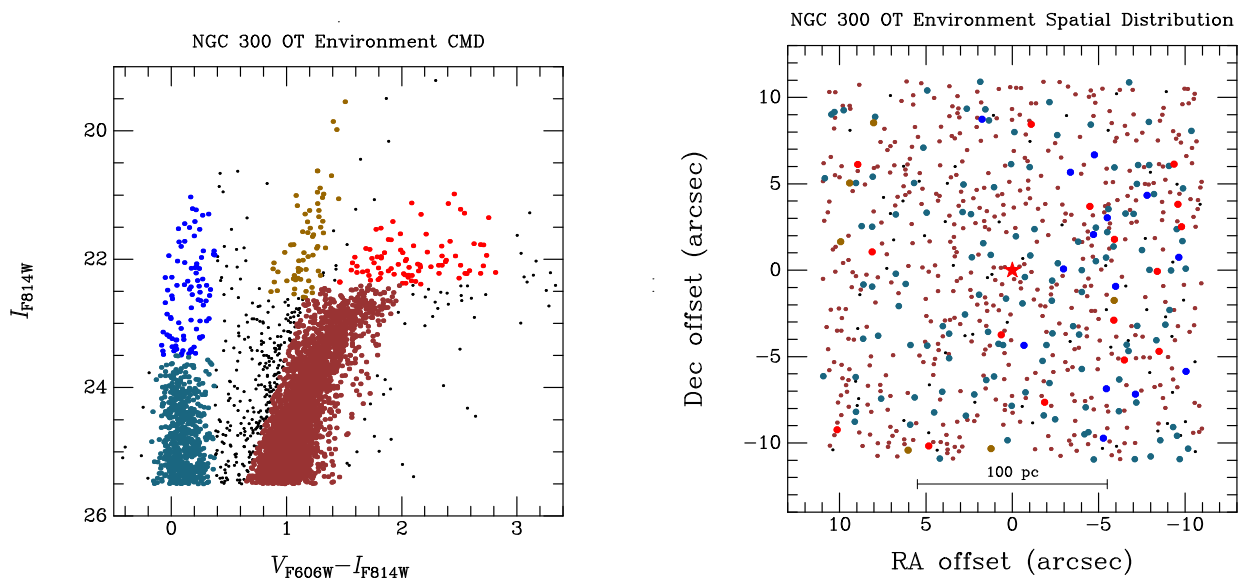


Fig. 4.— Left: The color-magnitude diagram for stars lying within a 500×500 pc square centered on the NGC 300 2008 OT. Color-coding; bright blue: bright main-sequence and blue-loop stars; slate blue: faint main-sequence stars; orange: red supergiants; bright red: AGB stars; dark red: red giants; black: all other stars in the field. Right: The spatial distribution of stars in a 200×200 pc square centered on the OT (represented by the large red star); same color-coding as in the left panel is used.

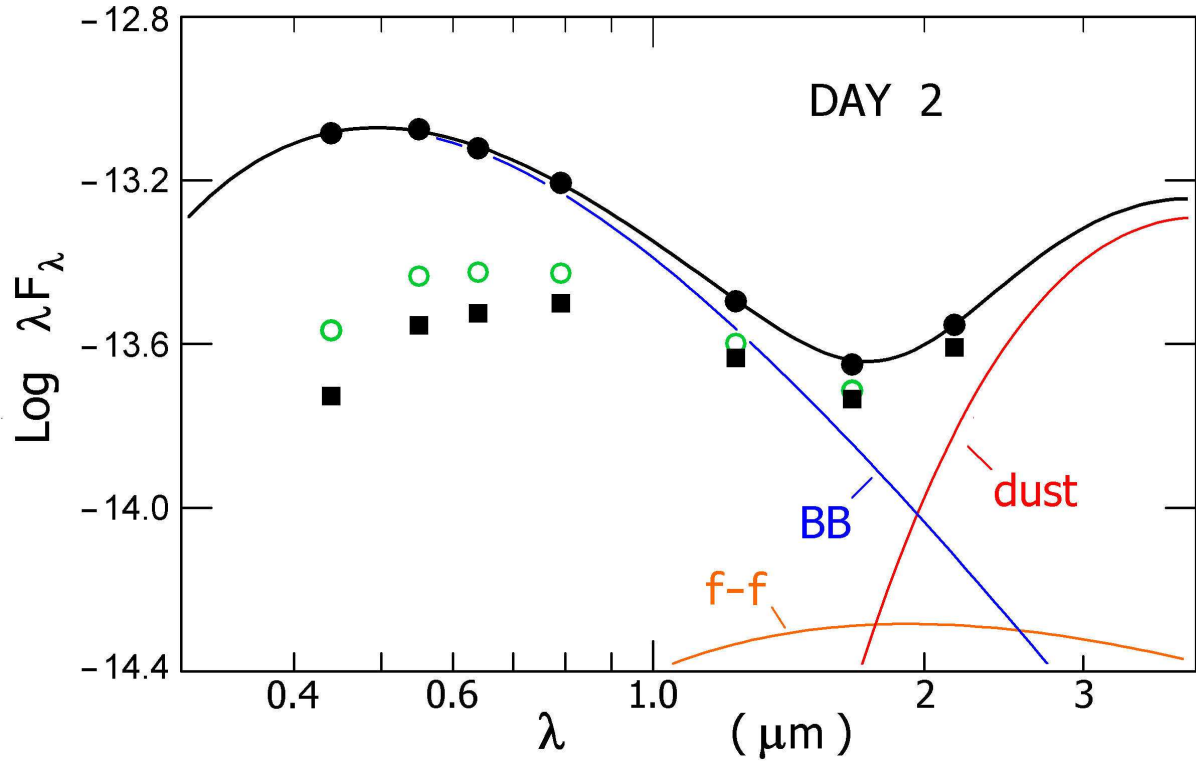


Fig. 5.— The spectral energy distribution, $\log \text{Watts m}^2$ vs. $\log \lambda$, at maximum light. The observed photometry is plotted as filled squares. The magnitudes corrected for the mean A_V and for $A_V = 1.2$ mag are shown as open and filled circles, respectively. The 7500 K blackbody for the latter points, the free-free contribution, and the 715 K dust are plotted separately. The combined contribution, the SED, is shown as a solid black line.

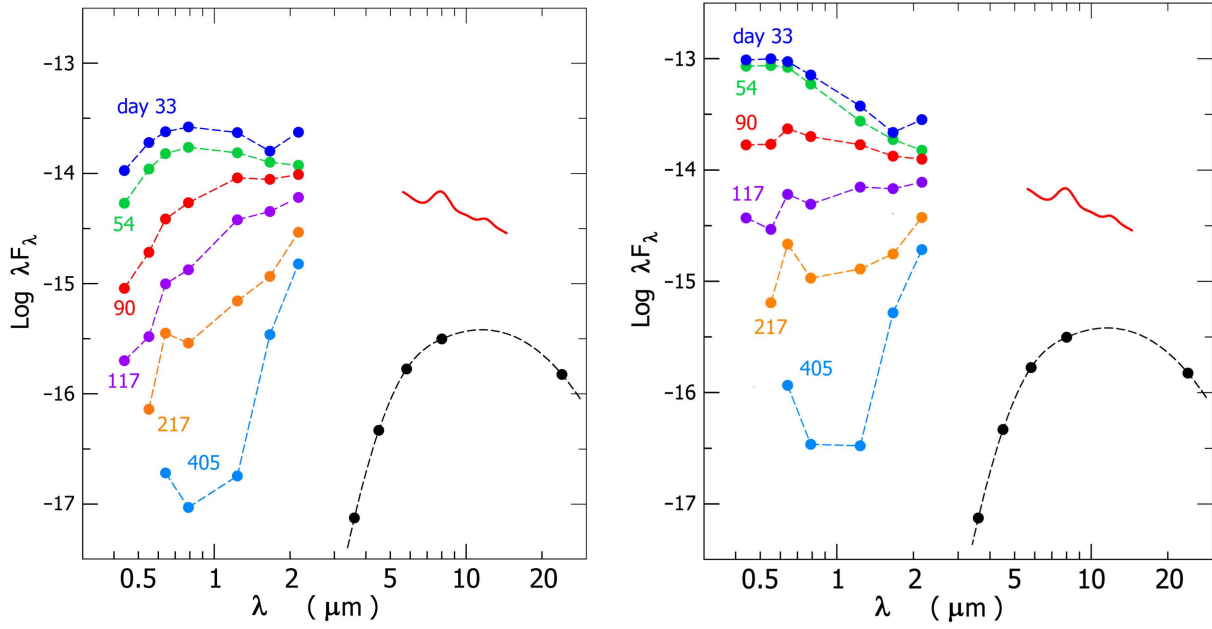


Fig. 6.— The evolution of the spectral energy distribution (\log Watts m^2 vs. $\log \lambda$) from day 33 to our last photometric observation with R and I magnitudes on 2009 June 6 (day 405). The observed magnitudes are plotted in the left panel and the SEDs corrected for extinction, as described in the text, are shown in the right panel. The mid-IR emission feature is shown with the day 90 photometry. The pre-eruption SED, in black, is also shown for comparison. The peak at R is due to strong $\text{H}\alpha$ emission. The extinction corrections used for the SEDs in the right panel are: day 33, $A_V = 1.8$, day 54, $A_V = 2.25$, day 90, $A_V = 2.37$.

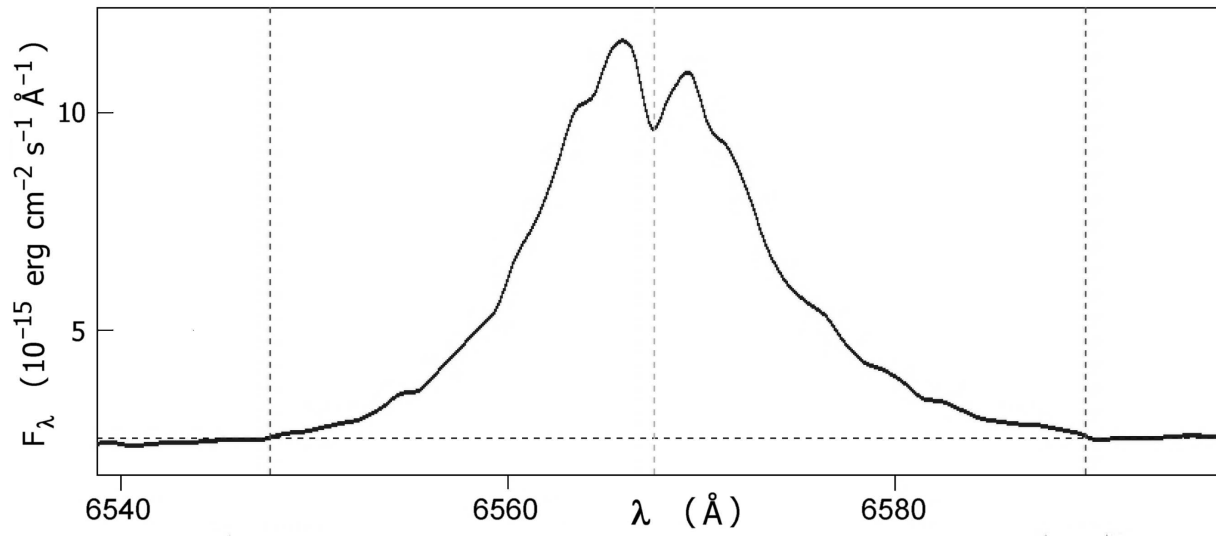


Fig. 7.— The H α line from 2008 July 6 showing the Thomson scattering wings. The dashed lines mark the blue and red extent of the wings and the center of the absorption minimum, see text. Also note the split profile with multiple components discussed in the text.

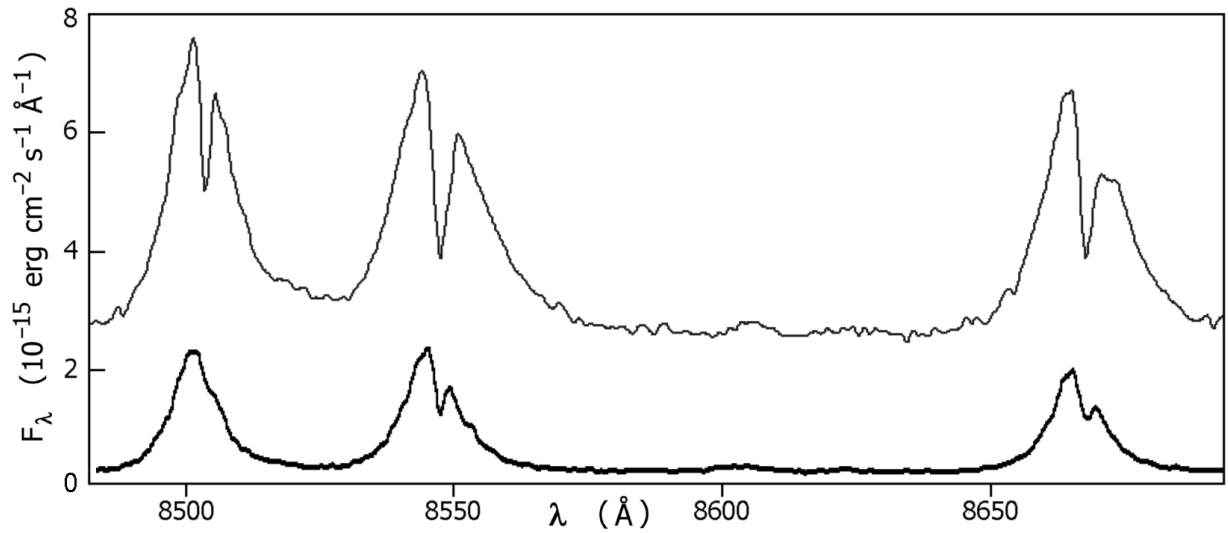


Fig. 8.— The Ca II triplet from 2008 July 6 (top) and August 30–September 1 (bottom), showing the evidence for multiple components and the variation in the profiles. The red emission component in the $\lambda 8498 \text{ \AA}$ line is no longer present in the echellette spectra from August 30 and September 1 and there is no clear absorption minimum, although a shoulder to the blue and red of the emission peak indicates the presence of additional emission. The other two lines in the triplet still show well-resolved double profiles. Also note the prominent redward wings similar to the [Ca II] lines in Figure 10.

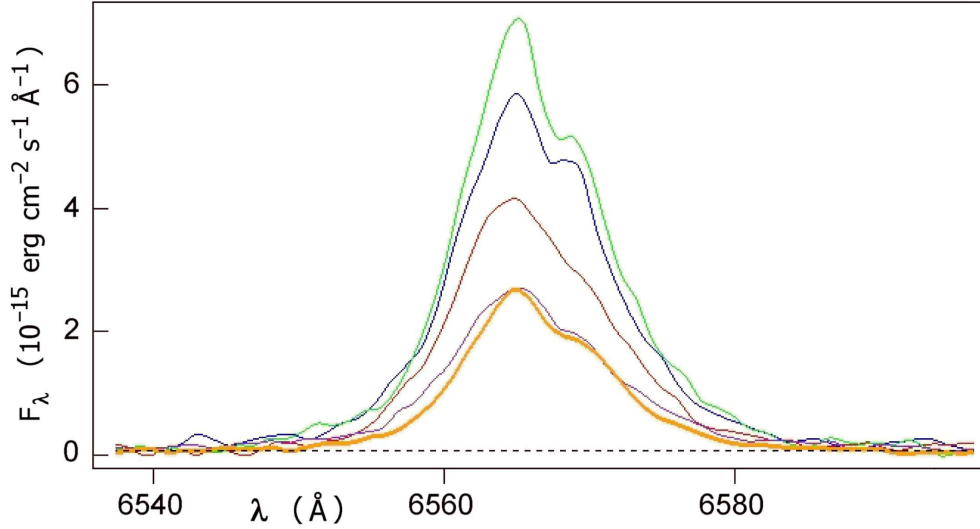


Fig. 9.— Variation in the appearance of the H α double-peaked profiles from 2008 Sep 10 to 2008 Oct 13. The profiles are color-coded by date: blue: Sep 10, red: Sep 13, green: Sep 16, purple: Sep 27, and gold: Oct 13.

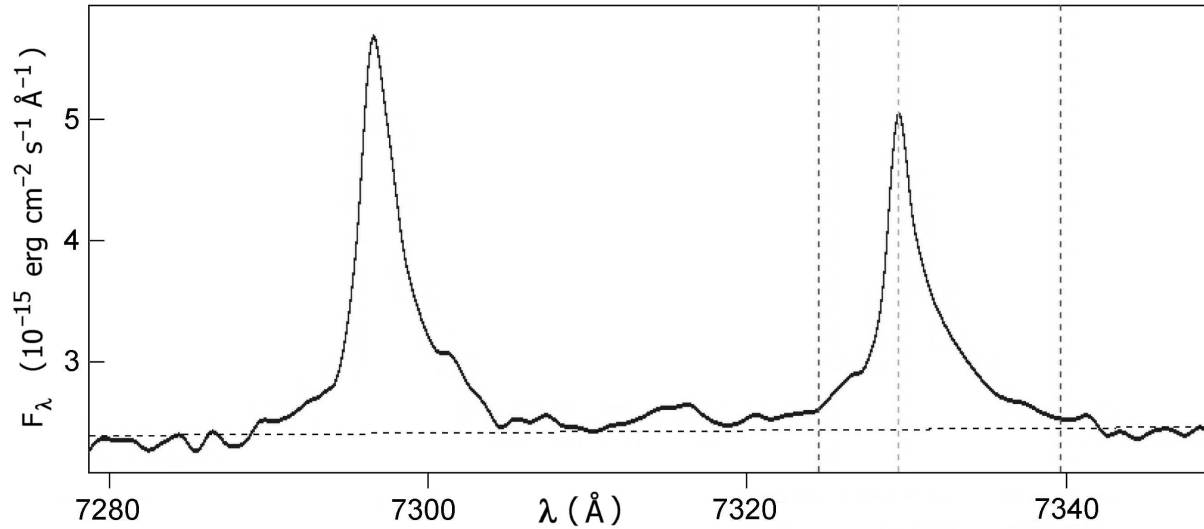


Fig. 10.— The [Ca II] lines from 2008 July 6, showing the asymmetric profiles and the Thomson scattering wings. The dashed lines mark the blue and red extent of the wings on the 7323 Å line.

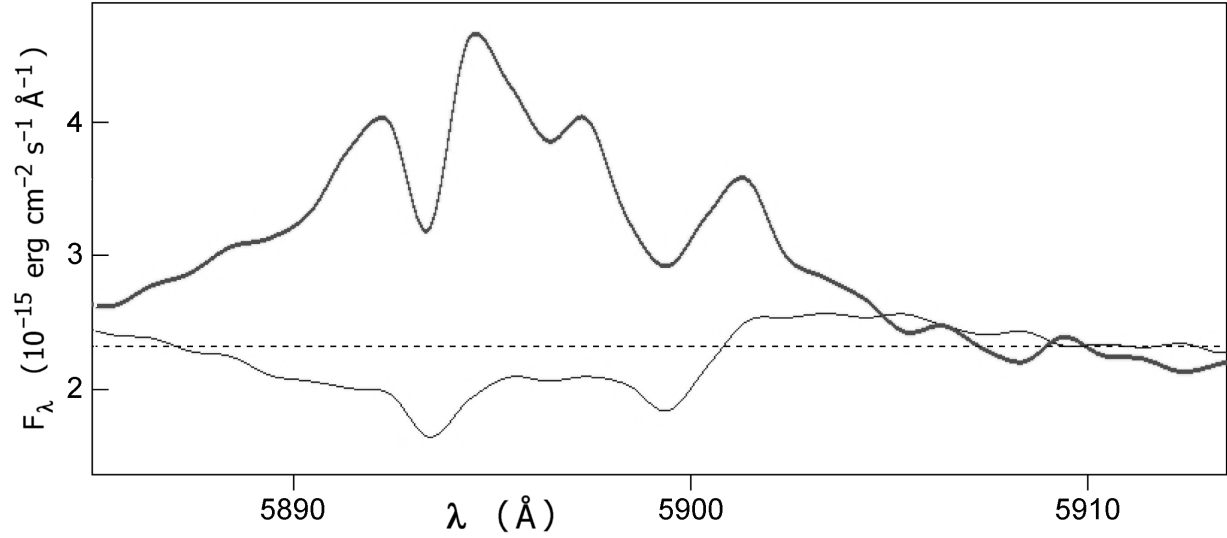


Fig. 11.— The Na I D lines transition from a pure absorption profile on 2008 Jul 6, the lower profile, to an emission profile with absorption on 2008 Aug 30, the upper, darker profile.

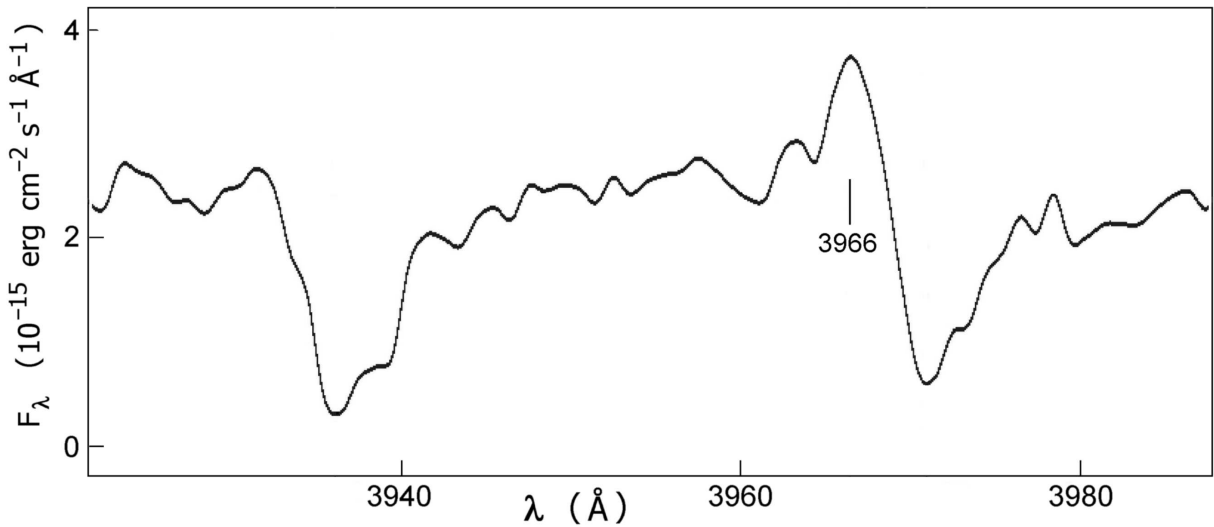


Fig. 12.— The Ca II H and K absorption lines from 2008 Jul 6 showing the double absorption profiles in each line. The emission line at 3966Å is a blend of He I λ 3964 and Fe II λ 3964.

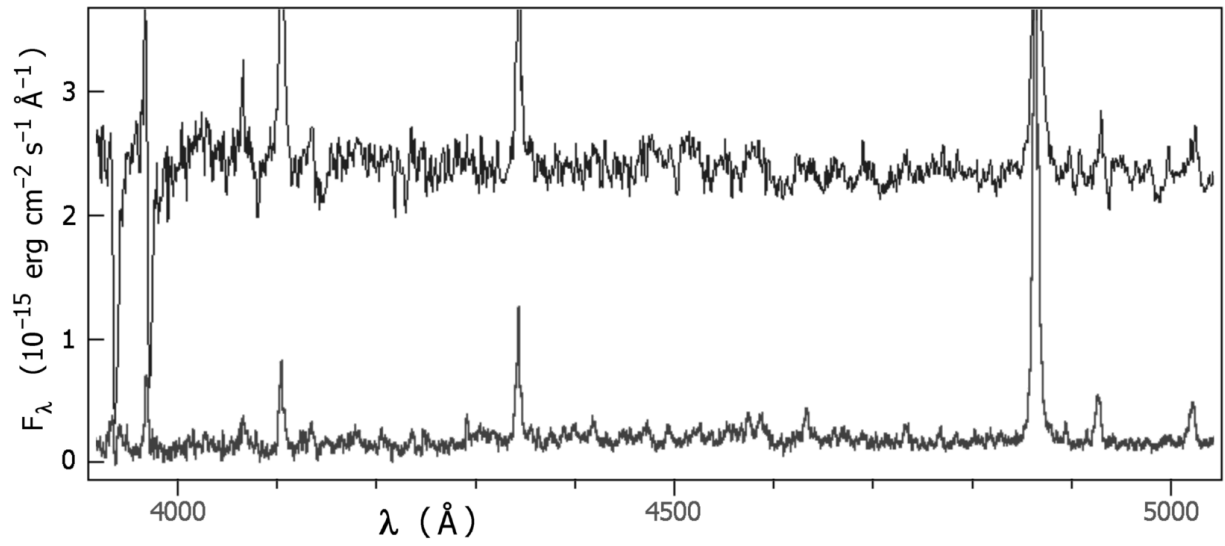


Fig. 13.— The echelette spectra in the blue from approximately Ca II H and K to 5000Å illustrating the change in the absorption line spectrum from 2008 Jul 6, upper spectrum, to 2008 Aug 30/Sep 01, the lower spectrum.

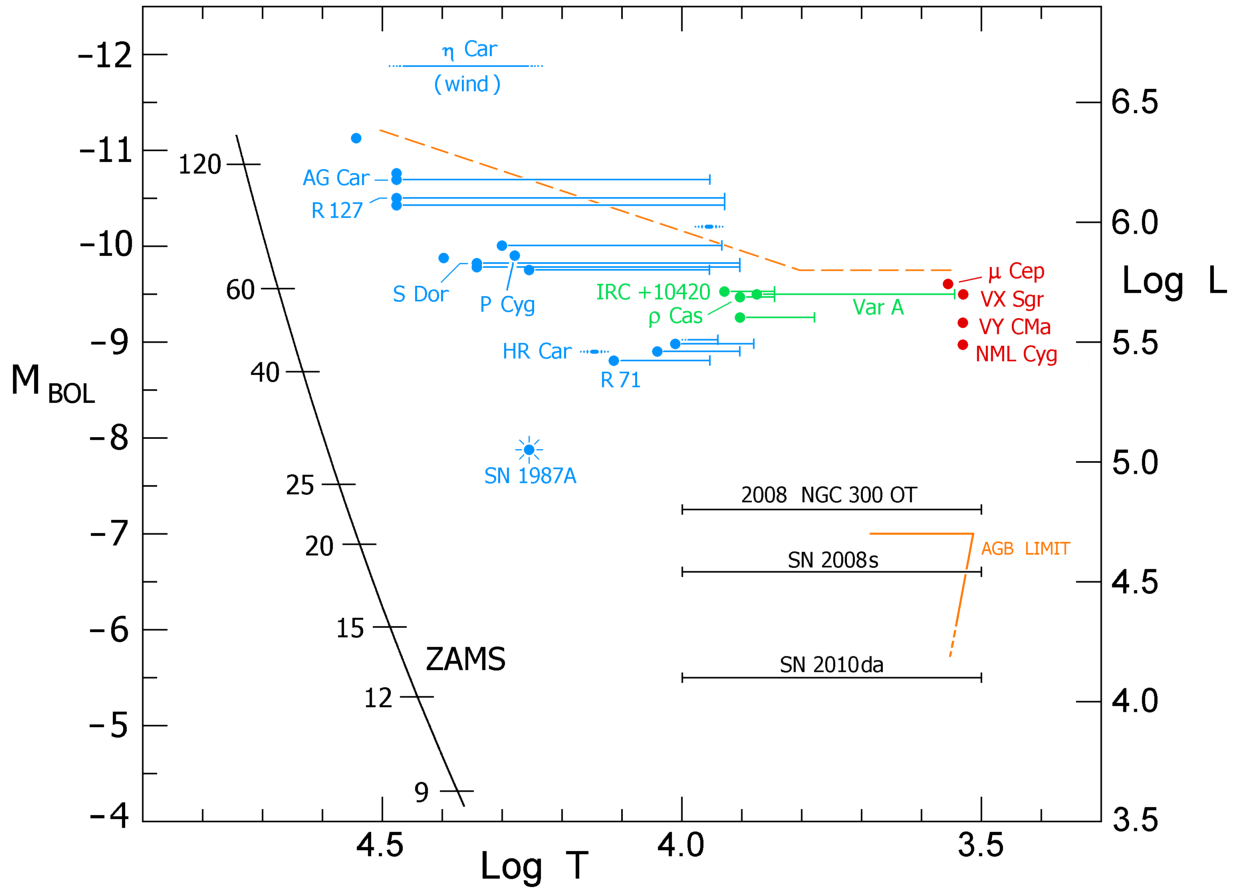


Fig. 14.— A schematic HR diagram showing the locations of the progenitors of NGC 300 OT2008-1, SN 2008S and SN 2010da. Several well-known unstable and high-mass-losing stars are also shown, including η Car and known LBVs, in blue with their transits in apparent temperatures during their optically thick wind stage or eruption, and the warm and cool hypergiants, in green and red, respectively. The empirical upper luminosity boundary is shown as a dashed line (see Humphreys & Davidson 1994).